Nanoscale Advances

ROYAL SOCIETY OF CHEMISTRY

REVIEW

View Article Online
View Journal | View Issue

Cite this: *Nanoscale Adv.*, 2020, **2**, 536

Two-dimensional metal–organic frameworks and their derivatives for electrochemical energy storage and electrocatalysis

Kuangmin Zhao,† Weiwei Zhu,† Suqin Liu,* Xianli Wei, Guanying Ye, Yuke Su and Zhen He *

Received 14th November 2019
Accepted 5th January 2020

DOI: 10.1039/c9na00719a

rsc.li/nanoscale-advances

Two-dimensional (2D) metal–organic frameworks (MOFs) and their derivatives with excellent dimension-related properties, *e.g.* high surface areas, abundantly accessible metal nodes, and tailorable structures, have attracted intensive attention as energy storage materials and electrocatalysts. A major challenge on the road toward the commercialization of 2D MOFs and their derivatives is to achieve the facile and controllable synthesis of 2D MOFs with high quality and at low cost. Significant developments have been made in the synthesis and applications of 2D MOFs and their derivatives in recent years. In this review, we first discuss the state-of-the-art synthetic strategies (including both top-down and bottom-up approaches) for 2D MOFs. Subsequently, we review the most recent application progress of 2D MOFs and their derivatives in the fields of electrochemical energy storage (*e.g.*, batteries and supercapacitors) and electrocatalysis (of classical reactions such as the HER, OER, ORR, and CO_2RR). Finally, the challenges and promising strategies for the synthesis and applications of 2D MOFs and their derivatives are addressed for future development.

1. Introduction

Advanced electrochemical energy storage and conversion technologies such as rechargeable batteries, supercapacitors, fuel cells, and electrolytic cells play crucial roles in the current energy systems.[1–3] The exploration of advanced electrode materials (*i.e.* electrochemical energy storage materials and electrocatalysts) with sufficient ion storage sites, excellent ion diffusion ability, high conductivity, and abundant active catalytic sites is vital but challenging.[4–6]

Metal–organic frameworks (MOFs), a series of crystalline materials consisting of metal ions and organic ligands,[7,8] have been extensively investigated for electrochemical energy storage[9–11] and electrocatalysis[12–15] due to their abundant active sites, tunable pore distribution, and controllable morphologies[7,16–23] Benefiting from the ordered arrangement of the

College of Chemistry and Chemical Engineering, Hunan Provincial Key Laboratory of Chemical Power Sources, Central South University, Changsha, Hunan 410083, P. R. China. E-mail: zhenhe@csu.edu.cn; sqliu2003@126.com

† Kuangmin Zhao and Weiwei Zhu contributed equally to this work.

Mr Kuangmin Zhao received his B.S. degree in Chemical Engineering and Technology (in 2013) at Sichuan University, Chengdu, Sichuan, China and M.S. degree in Chemical Engineering and Technology (in 2016) at Central South University, Changsha, Hunan, China. He is currently a Ph.D. candidate in Chemical Engineering and Technology at Central South University under the supervision of Prof. Suqin Liu and Prof. Zhen He. His research interests include the design and synthesis of two-dimensional materials for energy storage and conversion.

Mr Weiwei Zhu obtained his B.S. degree in Applied Chemistry (in 2016) and M.S. degree in Chemical Engineering and Technology (in 2019) at Central South University, Changsha, Hunan, China. He is currently a Ph.D. candidate in Chemical Engineering and Technology at Central South University under the supervision of Prof. Suqin Liu and Prof. Zhen He. His research is focused on the morphology and electronic structure-controlled synthesis of electrocatalysts for CO_2 reduction.

metal ions and organic linkers in the MOFs, the MOF derivatives tend to show a homogeneous distribution of the metal atoms or/and metal nanoparticles,[24,25] which could enhance the metal utilization efficiency[26] and further leads to a great improvement for their applications in energy storage and electrocatalysis. To date, carbon materials,[27] metals,[28] transition metal oxides,[25,29,30] transition metal carbides,[31] transition metal dichalcogenides,[32,33] transition metal phosphides,[34–36] and their composites[37] have been successfully fabricated from MOF precursors. It is well-known that the morphology of the electrode materials shows a correlation with the ion transport distance, which is a key factor that determines the ion transport resistance and then affects the ion diffusion ability.[38,39] However, MOFs with a bulk morphology usually possess a low metal utilization and accessible surface area as well as poor ion diffusion ability. To further enhance such properties of MOFs and MOF derivatives, great efforts have been devoted to fabricating low-dimensional MOFs with a controllable morphology and size towards a larger specific surface area and better ion diffusion properties.[40–42]

Since the discovery of graphene in 2004,[43–45] many two-dimensional (2D) materials, such as the nanosheets of porous carbon,[46–48] transition metal disulfides,[49,50] black phosphorus,[51,52] BN,[53] and Mxenes,[54] have been extensively investigated due to their unique structures and electronic properties. Ascribing to the distinctive dimension-dependent properties, such as high aspect ratios, abundant accessible active sites, and short ion transport distances, 2D MOFs,[55] as a new class of 2D materials, have fascinated researchers in various fields.[55–57] In addition, the inorganic metal compounds/C composites derived from 2D MOFs with a better conductivity are extensively investigated as energy storage materials and electrocatalysts.[58,59] Similar to other 2D materials, the properties of 2D MOFs and their derivatives greatly depend on the thickness.[60] Exploring efficient methods to prepare high-quality 2D MOFs with a desirable thickness is a main concern for the practical application of 2D MOFs.[61] To date, numerous synthetic methods have been developed to controllably synthesize 2D MOFs, which can be classified into two approaches, *i.e.*, top-down and bottom-up.[62] Generally, the top-down approach includes the physical and chemical/electrochemical exfoliation methods and the bottom-up approach includes the two-phase interfacial or intermediate layer growth methods, surfactant-assisted methods, molecule-precoordinated methods, template-assisted methods, and competitive coordination methods, *etc.*[33,63,64] 2D MOFs with excellent dimension-dependent properties have been widely employed as energy storage and electrocatalytic materials. More importantly, 2D MOF derivatives with better conductivity employed in energy storage and electrocatalysis are currently at a stage of rapid development.[65,66] Thus, a critical review focusing on the synthesis and application of 2D MOFs and their derivatives for electrochemical energy storage and electrocatalysis is highly demanded.

In this review, the synthetic strategies of 2D MOFs in recent years as well as the applications of 2D MOFs and their derivatives in energy storage and electrocatalysis are summarized. We start with the discussion on the representative synthesis of 2D MOFs and strategies of regulating the 2D MOFs' surface compositions and structural properties. Then, to better help the readers to understand the advantages of the 2D MOFs and their derivatives in energy storage and electrocatalysis, we thoroughly summarize suitable 2D MOFs and their derivatives for specific applications in batteries, supercapacitors (SCs), the oxygen evolution reaction (OER), hydrogen evolution reaction (HER), oxygen reduction reaction (ORR), and CO_2 reduction reaction (CO_2RR). Finally, the opportunities and challenges of the synthesis and application of the 2D MOFs are discussed.

2. Strategies for the synthesis of 2D MOFs

To date, 2D MOFs have been synthesized by various synthesis strategies. In this section, these reported synthesis strategies for

Prof. Suqin Liu received her Ph.D. degree in Applied Chemistry at Central South University, Changsha, Hunan, China. She is currently a professor in the College of Chemistry and Chemical Engineering at Central South University. Her primary research interests are focused on sustainable energy storage and conversion, including vanadium redox flow batteries, metal–air batteries, Li-ion batteries, and electrocatalysis. She has published over 240 papers in peer-reviewed journals, which have been cited over 4600 times.

Prof. Zhen He is currently an associate professor in the College of Chemistry and Chemical Engineering at Central South University, Changsha, Hunan, P. R. China. He received his B.S. degree in Materials Science and Engineering from Beijing University of Chemical Technology in 2006, and his Ph.D. degree in Chemistry from Missouri University of Science and Technology (formerly known as University of Missouri, Rolla), Rolla, Missouri, U.S., in 2012. His group is currently focused on designing, synthesizing, and understanding functional materials for applications in energy conversion and storage.

the 2D MOFs will be reviewed as two categories: top-down and bottom-up.[62]

2.1. Top-down approach

The top-down approach refers to a series of methods that synthesize the 2D materials from the corresponding bulk materials by breaking the interactions between the adjacent layers, which are commonly used for the fabrication of most of the 2D materials, such as graphene, transition metal dichalcogenides, and black phosphorus.[67] Layered bulk MOFs, in which the adjacent MOF layers are combined by the weak van der Waals forces and chemical bonds, can also be separated into 2D MOF nanosheets *via* the top-down approach including physical exfoliation and chemical/electrochemical exfoliation.

2.1.1. Physical exfoliation. The interlayer interactions in most of the layered bulk MOFs are the weak van der Waals forces and/or hydrogen bonds, which can be easily broken by external forces.[68] For such layered bulk MOFs, physical exfoliation, such as ball-milling, ultrasonication, and shaking, is considered as an efficient way to obtain their 2D form.

Previously, the layered bulk Zn(TPA)(H_2O)DMF and $[Cu_2Br(IN)_2]_n$ MOFs (TPA = terephthalic acid, DMF = *N*,*N*-dimethylformamide, and IN = isonicotinato) were exfoliated by ultrasonication. As shown in Fig. 1a, a single layer of Zn(TPA)(H_2O)DMF is constructed by the paddle-wheel Zn_2 clusters and terephthalates. In the bulk crystal, the Zn(TPA)(H_2O)DMF layers are held together by the hydrogen bonds between the H_2O and DMF intercalated in the interlayer (Fig. 1b).[69,71] The $[Cu_2Br(IN)_2]_n$ layer is constructed by bridging a copper dimer with a bromine ligand and isonicotinato linkers (Fig. 1d).[70] The four coordination bonds of Cu^{2+} are two Cu–O bonds and two Cu–N bonds. The π-stacking interactions between the isonicotinato aromatic rings in the adjacent layers lead to the stacking of the $[Cu_2Br(IN)_2]_n$ layers along the *a* axis in the bulk (Fig. 1e). After a simple ultrasonic treatment, 2D Zn(TPA)(H_2O)DMF and $[Cu_2Br(IN)_2]_n$ nanosheets with a thickness of about 2 and 0.5 nm, respectively, were successfully obtained (Fig. 1c and f). In addition, the ultrasonication method combined with suitable solvent interaction and substitution could be extended to synthesize other 2D MOFs. For example, the 3D cubic $Zn_4O(A)_3$ (A = 2,5-bis(3-methoxypropoxy)-1,4-benzenedicarboxylate) framework structure could be directly converted to the $Zn_4O(A)_3$ (DMF) nanosheets with a thickness of 0.94 nm by ultrasonication in a DMF solution due to the DMF being able to break the weak coordination between the Zn^{2+} and side-chain of the A.[72]

Compared to direct ultrasonication, wet ball-milling pretreatment combined with ultrasonication is a more efficient physical method for the exfoliation of layered bulk MOFs. Peng and co-workers employed a ball-milling pretreatment to ultrasonically exfoliate bulk $Zn_2(BIM)_4$ (Fig. 2a and b),[22] a layered MOF constructed by $Zn(BIM)_2$ chains cross-connected by Zn^{2+} in the *ab* plane and the weak van der Waals forces between the adjacent layers.[22] As shown in Fig. 2b, the interlayer distance of the adjacent $Zn_2(BIM)_4$ layers is about 0.988 nm, which is large enough for the insertion of small molecules for further exfoliation. The wet ball milling pretreatment provides a shear force to enlarge the

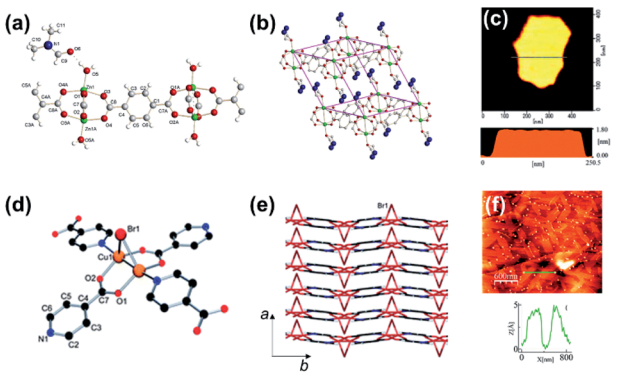

Fig. 1 (a) 2D layer structure of Zn(TPA)(H_2O)DMF with atom numbering. Note the distortion of the Zn_2O_8 units from the local D_{4h} point symmetry. (b) Layer structure of Zn(TPA)(H_2O)DMF with blue atoms depicting the DMF disorder. (c) AFM images and height profile of Zn(TPA)(H_2O)DMF nanosheets. Reproduced with permission.[69] Copyright©2011 The Royal Society of Chemistry. (d) Detailed view of the copper environment and (e) superposition of layers along the *a* axis in $[Cu_2Br(IN)_2]_n$. (f) AFM images and height profile of $[Cu_2Br(IN)_2]_n$. Reproduced with permission.[70] Copyright©2010 The Royal Society of Chemistry.

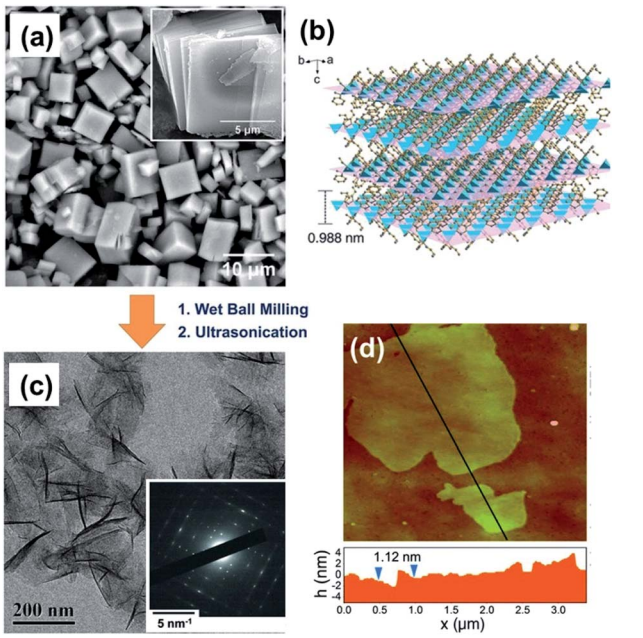

Fig. 2 (a) SEM image of as-synthesized $Zn_2(BIM)_4$ crystals. The inset image shows the typical flake-like morphology of $Zn_2(BIM)_4$ crystals. (b) Architecture of the layered MOF precursor. The *ab* planes are highlighted in purple to better illustrate the layered structure. (c) TEM image of $Zn_2(BIM)_4$ nanosheets. The inset shows the SAED image of $Zn_2(BIM)_4$. (d) Tapping-mode AFM topographical image of $Zn_2(BIM)_4$ nanosheets on silicon wafer. The height profile of the nanosheets along the black lines is marked in the image. Reproduced with permission.[22] Copyright© 2014 American Association for the Advancement of Science.

interlayer distance and intercalate more small molecules between the layers of $Zn_2(BIM)_4$. The low-magnification TEM image in Fig. 2c shows the $Zn_2(BIM)_4$ nanosheets obtained from the layered bulk $Zn_2(BIM)_4$ in a small-molecule solvent (*i.e.*, a mixture of methanol and propanol) under ultrasonication. The selected-area electron diffraction (SAED) pattern of a few-layer Zn_2BIM_4 nanosheet collected along the *c* axis (inset in Fig. 2c) matches with the diffraction pattern of the (110) planes of Zn_2BIM_4, indicating the well preserved crystallinity of the Zn_2BIM_4 nanosheets after the exfoliation. The thickness of the resulting Zn_2BIM_4 nanosheets measured by AFM is about 1.12 nm (Fig. 2d). The ball-milling pretreatment combined with ultrasonication could significantly improve the yield and quality of the 2D MOFs, therefore it has gradually replaced the sole ultrasonic exfoliation. Since the invention of this method, a number of layered MOFs constructed by the weak van der Waals forces between the layers have been exfoliated to the corresponding MOF nanosheets, *e.g.* Zn_2BIM_3 [65] and $[Cu(\mu\text{-}pym_2S_2)(\mu\text{-}Cl)]_n \cdot n$MeOH ($pymS_2$ = dipyrimidindisulfide).[73]

2.1.2. Chemical/electrochemical exfoliation. Chemical exfoliation is also considered as a potential method for preparing 2D MOFs from layered bulk MOFs, especially for pillared-layer type MOFs. For instance, Jiang and co-workers embedded the chemically labile dipyridyl ligand, 4,4-dipyridyl disulfide (DPDS), into the layered $Zn_2(PdTCPP)$ crystals to form a new intercalated MOF, $Zn_2(PdTCPP)(DPDS)_2$ (Fig. 3a).[74] Then, the disulfide bond was reduced and broken by trimethylphosphine (TMP), resulting in ultrathin $Zn_2(PdTCPP)(DPDS)_2$ nanosheets with a high yield of 57%, which was the highest yield reported for MOF nanosheets from the exfoliation of the bulk MOFs. The TEM and AFM images (Fig. 3b–d) show that the freestanding $Zn_2(PdTCPP)(DPDS)_2$ nanosheets have lateral sizes of up to micrometers and a thickness of about 1 nm. The HRTEM image (Fig. 3e) shows that the lattice fringe of the $Zn_2(PdTCPP)(DPDS)_2$ nanosheet is 1.65 nm, which corresponds to the (100) plane of the intercalated MOF crystal. Similarly, some other labile linkers or linkers with a weak coordination ability were used to exfoliate the bulk MOFs. Inspired by the unusual behavior of formic acid, a modulator in other RCOO-containing MOFs,[76] Grey and co-workers found that the ratio of metal centers and organic linkers could be well controlled by adding formic acid, forming two different Hf-containing MOFs, *i.e.* fcc UiO-67 and hcp UiO-67 (Fig. 3f).[75] More importantly, the hafnium oxide nodes in hcp UIO-67 could form a double cluster ($Hf_{12}O_8(OH)_{14}$) and release lots of ligand deficiencies. On grinding or sonication, hcp UiO-67 was converted to 2D MOF nanosheets (hxl UiO-67) (Fig. 3g). The TEM image of hxl UiO-67 confirms its nanosheet nature (Fig. 3h) and the TEM image of the edge of the as-obtained hxl UiO-67 shows that the thickness of these nanosheets is 11 ± 1 nm (Fig. 3i), corresponding to four times the lattice parameter of the unit cell of hxl UiO-67. Although chemical exfoliation is the most efficient top-down method to fabricate 2D MOF nanosheets with a high quality and reasonable yield, it requires that the precursor MOF bulk must possess uncoordinated metal sites, which has limited its universality.

Since most of the pillared-layer type MOFs are stable enough under various reaction conditions, selective breaking of the coordination bonds between the layers is still challenging. More recently, the electrochemical oxidation method was also employed to exfoliate the pillared-layer type MOFs. By selecting the pillar ligand with a redox active backbone that can be selectively oxidized and removed, the pillared-layer type MOFs can be easily exfoliated to 2D MOF nanosheets. As shown in Fig. 4a, Zhang reported an electrochemical exfoliation strategy relying on the covalent modification of the pillar ligands.[77] In detail, $H_2[Co_6O(dhbdc)_2(H_2dhbdc)_2(EtOH)_4]_2(EtOH{-}H_2O)$ (denoted as MCF-13 or 3D-Co) was synthesized by treating $Co(CH_3COO)_2$ and 2,3-dihydroxy-1,4-benzenedicarboxylic acid

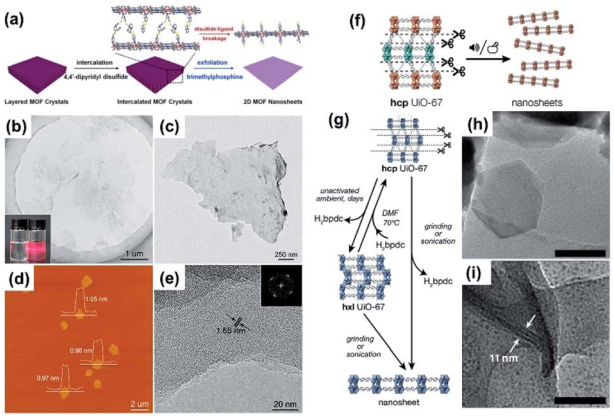

Fig. 3 (a) Schematic illustration of the process developed to produce 2D MOF nanosheets *via* an intercalation and chemical exfoliation approach. (b) TEM image of the exfoliated MOF nanosheets. Inset: Tyndall effect (left) before and (right) after exfoliation. (c) TEM image of an individual exfoliated MOF nanosheet. (d) AFM image of the exfoliated MOF nanosheets with corresponding height profiles. (e) High-resolution TEM image of an exfoliated multilayer MOF nanosheet. The corresponding FFT pattern is shown in the inset. (f) Illustration of the preparation of hxl UiO-67 nanosheets. (g) Schematic illustration of the chemical transformation of hcp UiO-67 to hxl UIO-67 and UIO-67 nanosheets. (h) TEM and (i) HRTEM images of UIO-67 nanosheets. Reproduced with permission.[74,75] Copyright©2017 American Chemistry Society.

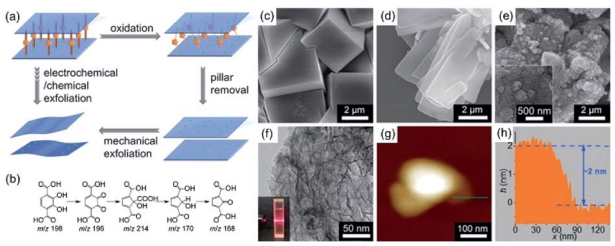

Fig. 4 (a) Illustration of the synthetic process of 2D MOFs by using the electrochemical/chemical exfoliation method and (b) a possible oxidative transformation route from H_4dhbdc to a species with *m*/*z* 168. SEM images of (c) 3D-Co, (d) 2D-Co, and (e) 2D-Co-NS. (f) TEM image of 2D-Co-NS (inset: Tyndall effect of a colloidal solution). (g) AFM image and (h) the corresponding height profile of 2D-Co-NS. Reproduced with permission.[77] Copyright©2018 WILEY-VCH Verlag GmbH & Co. KGaA.

(H_4dhbdc) mixed solution in an autoclave at 140 °C for 72 h. The electrochemical exfoliation strategy could directly remove the pillar ligands (H_4dhbdc) in the 3D-Co and afford the 2D Co_6-$O(dhbdc)_2(OH)_2(H_2O)_{10}$ nanosheets (2D-Co-NS) without additional complex processes. Fig. 4b illustrates the possible oxidative transformation route from the H_4dhbdc pillar ligand (*m*/*z* 198) to a pillar ligand with *m*/*z* 168, which could significantly lower the coordination ability of $-COO^-$ in the pillar ligands and facilitate the removal of the pillar ligands by the solvent. Fig. 4c–e show the morphology evolution from 3D-Co to 2D-Co-NS. The TEM image (Fig. 4f) shows that 2D-Co-NS has a wrinkled nanosheet morphology and the AFM image (Fig. 4g) and height profile (Fig. 4h) show that the thickness of the 2D-Co-NS is only about 2 nm.

The top-down approach, with the advantages of simplicity and low-cost, has been widely used for the synthesis of 2D MOF nanosheets from the layered bulk MOFs with relatively large interlayer distances and/or weak coordination ability. The yield of the 2D MOFs in the top-down approach greatly depends on the structural properties of the bulk MOF precursors. The relatively low yield of the 2D MOF nanosheets derived from the bulk MOFs by the top-down approach gives rise to inhomogeneous products, which requires troublesome separation processes and therefore has hindered the practical application of the top-down approach.[78] Thus, the development of the top-down approach is much slower than that of the bottom-up approach, which will be discussed in the next section.

2.2. Bottom-up approach

The bottom-up approach, which fabricates the 2D MOF nanosheets by directly assembling the organic linkers and metal ions *via* coordination interactions, has been intensively investigated in the past few years because it can facilely control the growth of the 2D MOF nanosheets with various functional metal nodes and thicknesses. A key point of the bottom-up approach for the fabrication of 2D MOFs is to control the growth rate of the MOF crystals along certain directions. Compared to the top-down approach, the bottom-up approach is considered to be more efficient to fabricate the 2D MOFs with better homogeneity.[79] Based on the synthesis mechanism, the bottom-up approach can be classified into four categories: template-assisted method, interface or intermediate layer growth method, surfactant-assisted method, and molecule-precoordinated method.

2.2.1. Template-assisted methods. In the template-assisted synthesis, the nucleation and growth of the target materials are on the surface of a template, which has been widely used for the synthesis of many 2D materials, such as graphene,[80] porous carbon nanosheets,[81] and TMD nanosheets.[82] The 2D MOFs could also be bottom-up synthesized by different template-assisted methods including the hard-template method and sacrificial-template method.[83]

The hard-template method is a conventional method to controllably deposit the target materials on an unreacted substrate, in which the morphology of the target materials could be regulated by the surface properties of the substrate. A great advantage of the hard-template method for the synthesis of 2D MOFs is that by selecting suitable substrates the growth of the 2D MOFs can be controlled as nanosheet arrays,[84,85] which is significant for their application in gas separation. Besides, the introduction of the conductive substrates could also overcome some shortcomings of the 2D MOFs such as low conductivity and agglomeration. For instance, Li and coworkers chemically deposited 2D leaf-like ZIF (ZIF-L) arrays on a halloysite nanotube (HNT) coated PAN membrane.[84] As shown in Fig. 5a, in order to controllably grow the ZIF-L nanosheets, a uniformly oriented poly(sodium-*p*-styrenesulfonate)–HNT (PSS–HNT) layer was coated on the PAN membrane with PVA as the binder, then the ZIF-L was selectively deposited on the PSS–HNT-coated PAN membrane. More importantly, the authors found that the good arrangement of the HNTs was a vital factor for obtaining the ZIF-L nanosheet arrays, which can regulate the growth direction of the ZIF-L nanosheets due to the abundant surface functional groups and large surface area of the HNTs. The SEM (Fig. 5b) and EDS mapping (Fig. 5c) images show that the ZIF-L nanosheets are vertically grown on the HNT-coated PAN membrane. However, the thickness of the ZIF-L nanosheets prepared by this method is about 80 nm due to that there is no sufficient force to restrict the growth along the out-of-plane orientation of the nanosheets, which is a common shortcoming for the hard-template method to prepare the 2D materials.[86]

The sacrificial-template method, such as the *in situ* conversion of 2D metal oxides or hydroxides to 2D MOF nanosheets,

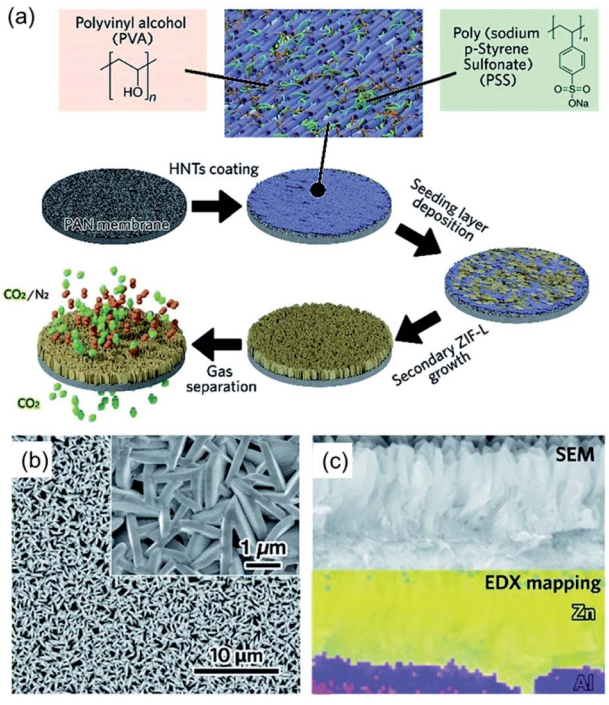

Fig. 5 (a) Schematic illustration for the preparation of the PAN–HNTs–ZIF-L membrane. (b) SEM image of the top-surface of the PAN–HNTs–ZIF-L membrane, and (c) EDS mapping and reference SEM image of the PAN–HNTs–ZIF-L membrane cross-sectional region. Reproduced with permission.[84] Copyright©2019 The Royal Society of Chemistry.

has also been intensively investigated in recent years. Wang and coworkers developed an *in situ* transformation strategy to synthesize ultrathin bimetal-MOF nanosheet (BMNS) arrays from layered double hydroxide nanosheets (LDH NSs) on conductive substrates (Fig. 6a).[87] Specifically, the LDH NSs were pre-deposited on the carbon clothes (Fig. 6b) and worked as a self-sacrificial template providing metal ions for the growth of BMNSs. The as-prepared LDH NSs were placed in 4 mL of DMF/H_2O (6 : 1, v/v) mixed solvent containing a certain amount of H_2BDC as the ligand. The deprotonated H^+ from H_2BDC could slowly react with the LDH NSs to release the metal ions which were *in situ* coordinated with the BDC linkers to form the ultrathin NiCo-BDC BMNSs (Fig. 6c). The XRD pattern (Fig. 6d) and TEM images (Fig. 6e and f) reveal the successful preparation of the BMNSs. The thickness of the BMNSs measured by AFM is about 5 nm (Fig. 6g). Moreover, the authors also found that the water content in the solution in which the conversion occurred was vital to the thickness of the BMNSs (Fig. 6g–i). This sacrificial-template method is considered as a general method for the conversion of metal LDH or metal oxide NSs to the M-MOF nanosheets (M refers to the metal in the precursors), which has been used in the fabrication of other MOF nanosheets from the corresponding metal LDH and oxide nanosheets.[88]

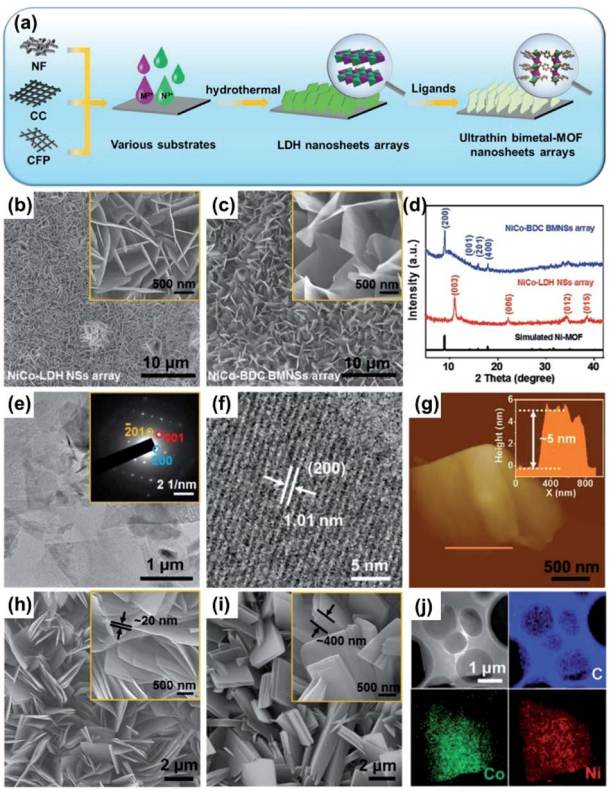

Fig. 6 (a) Schematic illustration showing the fabrication of ultrathin BMNS arrays on the 3D conductive matrix. SEM images of (b) NiCo–LDH NSs and (c) NiCo-BDC BMNS arrays (the insets are the corresponding high-magnification SEM images). (d) XRD patterns of NiCo-BDC BMNS arrays and pristine NiCo–LDH NS array. (e) TEM, (f) HRTEM, (g) AFM images and (j) EDS mapping of NiCo-BDC BMNS. (Inset of (e): the SAED pattern of a single BMNS; inset of (g): the corresponding height profile measured along the yellow line). SEM images of NiCo-BDC BMNSs with different thicknesses synthesized at (h) DMF : H_2O = 6 : 1 and (i) DMF : H_2O = 4 : 1 (the insets are the high-magnification SEM images). Reproduced with permission.[87] Copyright©2019 WILEY-VCH Verlag GmbH & Co. KGaA.

2.2.2. Two-phase interfacial or intermediate layer growth methods. The two-phase interfacial growth method was exploited at the initial stage of the development of the bottom-up approach for the synthesis of 2D MOFs. In the two-phase interfacial growth method, the metal ions and organic linkers are assembled at the liquid–liquid, liquid–gas, solid–gas, or solid–liquid interfaces. A crucial point of this method for the synthesis of 2D MOFs is to construct a suitable interface with a sufficient reaction area and adaptable ion- or molecule-diffusion ability so as to assemble the extended nanosheets while the metal ions and organic linkers diffuse from different phases to the interface.[89] Early in 2003, inspired by the chemical vapor deposition, Fe(trimellitic acid) nanosheets were assembled by the solid–gas interfacial growth method on the surface of Cu(100).[76] However, some of the critical synthesis conditions, such as the flat metal surface, high vacuum, and high energy input, hampered the development of the solid–gas interfacial growth method in the fabrication of the 2D MOF nanosheets. Thus, solid–liquid, liquid–gas, and liquid–liquid interfacial growth methods with milder synthesis conditions have attracted more attention than the solid–gas interfacial growth method for the synthesis of the 2D MOF nanosheets in recent years.

In 2010, Makiura invented a liquid–liquid interfacial growth method and prepared a preferentially oriented MOF nanofilm on a solid surface.[90] As shown in Fig. 7, the synthesis procedure involved spreading a solution of the molecular building units, 5,10,15,20-tetrakis(4-carboxyphenyl)porphyrinato-cobalt(II) (CoTCPP) and pyridine (py), in chloroform/methanol onto an aqueous solution of $CuCl_2 \cdot 2H_2O$, leading to the formation of a 2D copper-mediated CoTCPP array (CoTCPP-py-Cu) at the liquid–liquid interface.[90] Then, the single-layer CoTCPP-py-Cu was layer-by-layer transferred to the surface of a Si(001) substrate, resulting in a nanofilm constructed with highly oriented 2D CoTCPP-py-Cu MOF nanosheets. Later, the Kitagawa group developed a variety of interfacial synthetic methods combining the Langmuir–Blodgett method.[91–93] The key point of these methods is to well disperse the oil layer containing

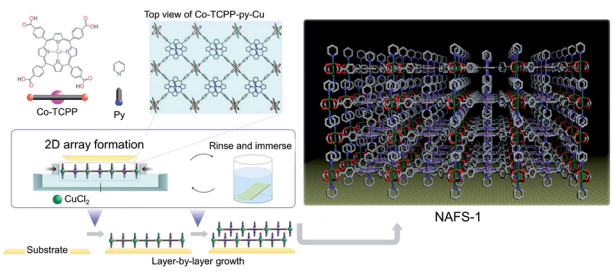

Fig. 7 Schematic illustration of fabrication method of NAFS-1. Reproduced with permission.[90] Copyright©2010 Nature Publishing Group.

organic linkers on the surface of an aqueous solution containing the metal ions, while the 2D MOFs could form as the metal ions diffuse to the oil layer and coordinate with the organic linkers.

Nowadays, the liquid–liquid interfacial growth strategy is the most useful method among all the reported two-phase interfacial growth methods for the 2D MOFs. Huang and co-workers demonstrated that a 2D π–d conjugated MOF, Cu-BHT (BHT = benzenehexathiol), could be assembled at the interface of the BHT/dichloromethane and aqueous copper(II) nitrate solutions, as shown in Fig. 8a and b.[94] The SEM images (Fig. 8c–e) show that the Cu-BHT film with a thickness of about 200 nm has been constructed by the stacking of the Cu-BHT nanosheets. More attractively, the conductivity of this as-assembled Cu-BHT film at room temperature could reach up to 1580 S cm^{-1}, which was the highest value ever reported for the conductive coordination polymers. These highly conductive 2D Cu-BHT nanosheets delivered excellent performance in electrochemical energy storage and electrocatalysis. However, this liquid–liquid method has an obvious shortcoming, that is, the later-formed Cu-BHT nanosheets are less ordered, leading to a rougher surface and lower conductivity (Fig. 8d and e). The authors mainly attributed this issue to the weaker interface-confining effect when the film grew thicker (Fig. 8f). To minimize the possible negative impact of the disordered arrangement of the Cu-BHT nanosheets, the reaction time should be carefully controlled to obtain the Cu-BHT film with an ordered surface. As discussed above, the liquid–liquid interfacial growth is a handy and concise method for directly assembling the 2D MOF nanosheets by only using the metal ions and organic linkers in suitable solvents. Unfortunately, the yield of the 2D MOF nanosheets by using the liquid–liquid interfacial growth method is usually quite low due to the small reaction area, which hinders their further applications.

To overcome the low yield of the 2D MOF nanosheets due to the small reaction area in the liquid–liquid interfacial growth method,[95,96] Rodenas and co-workers presented an intermediate layer growth method, in which the reaction solution consisted of three different liquid layers vertically stacked according to their densities, to generate 2D MOF nanosheets in the intermediate miscible co-solvent layer (Fig. 9). To emphasize this approach, the synthesis of the Cu-based 1,4-benzenedicarboxylate (CuBDC) MOF is selected as a showcase.[97] In this case, the upper solution layer containing $Cu(NO_3)_2$ ($DMF : CH_3CN$ = 1 : 2, v/v) and the lower solution layer containing BDC ($DMF : CH_3CN$ = 2 : 1, v/v) were separated by an intermediate solution layer ($DMF : CH_3CN$ = 1 : 1, v/v) (Fig. 9a). Under static conditions, the Cu^{2+} ions and BDC linker molecules slowly diffused into the intermediate solution layer, where the CuBDC MOF crystals formed locally in a highly diluted medium. This intermediate solution layer provided a sufficient reaction zone to form 2D CuBDC MOFs and the nascent 2D CuBDC crystals were naturally removed from the reaction zone by sedimentation, after which further growth of the CuBDC crystals was inhibited in the Cu^{2+}-depleted underlying organic phase (Fig. 9b). The SEM (Fig. 9c) and AFM (Fig. 9d) results show that the as-fabricated Cu-BDC nanosheets have lateral dimensions of 0.5–4 μm and thicknesses in the range of 5–25 nm. Besides, this intermediate layer growth method could also be extended

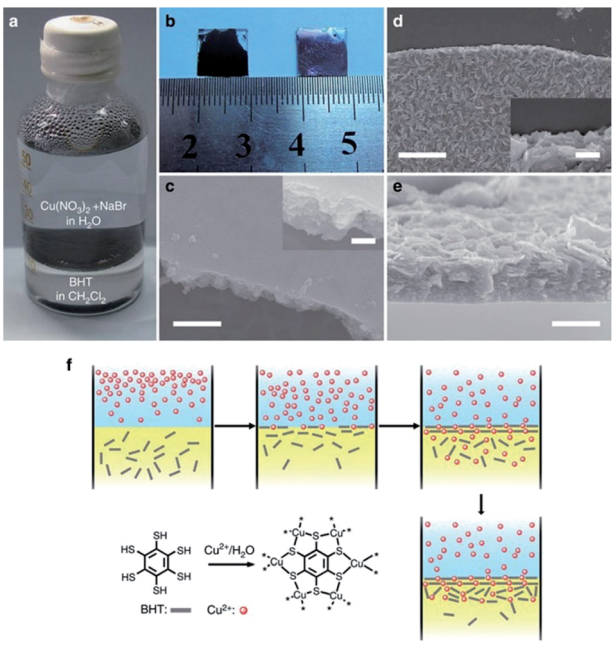

Fig. 8 (a) Photograph of the Cu-BHT film forming at the interface between an aqueous solution and CH_2Cl_2. (b) Photograph of upside-up (right) and upside-down (left) films transferred on glass substrates. The SEM image of (c) upside, (d) downside surface and (e) cross-section of a 200 nm-thick film. The insets in (c and d) show the details of the film edge at an enlarged scale. Scare bar, 200 nm in (c), 400 nm in (d and e) and 100 nm in the insets. (f) Scheme of the formation of Cu-BHT film. Reproduced with permission.[94] Copyright©2015 Nature Publishing Group.

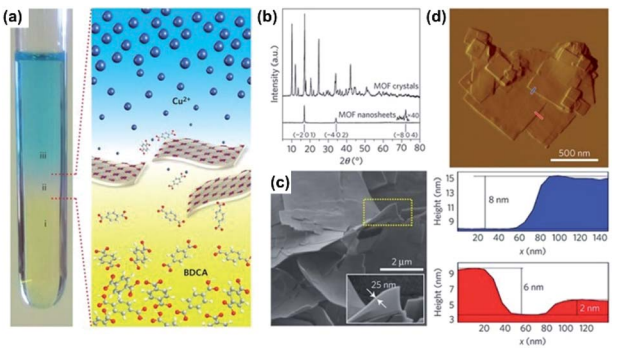

Fig. 9 (a) Picture showing the spatial arrangement of different liquid layers during the synthesis of CuBDC MOF nanosheets. Layers labelled (i), (ii) and (iii) correspond to a benzene 1,4-dicarboxylic acid (BDCA) solution, the solvent spacer layer and the solution of Cu^{2+} ions, respectively. (b) X-ray diffractograms (Cu K radiation) for the bulk-type and nanosheet CuBDC MOF. (c and d) Scanning electron micrograph and atomic-force micrograph (with corresponding height profiles), respectively, for CuBDC MOF nanosheets synthesized as illustrated in (c). The height profiles, color-coded red and blue, are measured along the corresponding tracks shown in the atomic-force micrograph. Reproduced with permission.[97] Copyright©2010 Nature Publishing Group.

to synthesize other ultrathin 2D MOFs, such as nanosheets of Zn-BDC, Co-BDC, copper 1,4-naphthalenedicarboxylate (Cu(1,4-NDC)), and copper 2,6-naphthalenedicarboxylate (Cu(2,6-NDC)).[97]

2.2.3. Surfactant-assisted methods. Compared to the template and interfacial growth methods which generally fabricate relatively thick (>10 nm) 2D MOFs with a relatively low yield (<10%), the direct synthesis of the 2D MOFs from homogeneous solutions with the assistance of certain surfactants is considered as an intriguing approach to fabricate 2D MOF nanosheets with a high yield and low thickness (<10 nm). The key to this synthesis approach is to inhibit the growth of the MOF crystals along a certain direction. During the growth of the MOF crystals, the surfactants selectively attach to certain crystallographic planes of the MOF crystals to suppress the crystal growth along the normal direction of the crystallographic plane, which leads to the formation of a 2D MOF structure. Zhang and co-workers synthesized a series of M-TCPP (M = Zn, Cu, Co, Ni, and Mg) nanosheets by using a polyvinylpyrrolidone (PVP)-assisted method.[86] As illustrated in Fig. 10a, a Zn-TCPP nanosheet is constructed by the TCPP ligands linked with $Zn_2(COO)_4$ metal nodes. During the synthesis, PVP could coordinate with the Zn^{2+} sites and hinder the interaction between the two separate 2D Zn-TCPP nanosheets. Further characterizations show that the Zn-TCPP nanosheets have a lateral size of 1.2 ± 0.4 μm and a thickness of 7.6 ± 2.6 nm (Fig. 10b–e). Other surfactants, such as cetyltrimethylammonium bromide (CTAB), and sodium lauryl sulfate (SLS),[66,98,99] have also been proved to be effective for the synthesis of 2D MOF nanosheets (Fig. 10f–k). Obviously, the uniformity and thickness of the 2D MOF nanosheets prepared by using the surfactant-assisted methods in homogeneous solutions are both significantly improved compared to that produced by the interfacial reaction. However, it could be hard to remove the surfactants attached on the surface of the 2D MOF nanosheet products by just washing. The attached surfactants would block most of the external active sites of the 2D MOF nanosheets produced by the surfactant-assisted methods, which hinders their applications in catalysis and energy storage.

2.2.4. Molecule-precoordinated methods. In addition to the surfactant-assisted method, molecule-precoordinated methods have also been used to directly obtain ultrathin 2D MOF nanosheets from homogeneous solutions. Previously, Lin and co-workers employed $HCOO^-$ to protect six of the twelve connection sites of a Hf_6 cluster (Fig. 11a).[100] The remaining six uncoordinated connection sites in the same plane were then coordinated with benzene-1,3,5-tribenzoate (BTB) to form $Hf_6(\mu_3\text{-}O)_4(\mu_3\text{-}OH)_4\text{-}(HCO_2)_6(BTB)_2$ MOF nanosheets.[100] Fig. 11b and c show that these MOF nanosheets have a thickness of 1.2 nm, corresponding to a single layer of the $Hf_6(\mu_3\text{-}O)_4(\mu_3\text{-}OH)_4\text{-}(HCO_2)_6(BTB)_2$ MOFs.

Recently, our group developed a series of small molecule-precoordinated methods for the synthesis of 2D MOF nanosheets.[101–103] The key to this method is to pre-coordinate the metal ions with certain small molecules, consequently slowing down the reaction rate between the metal ions and organic linkers. Besides, the small molecules attached on the surface of the as-prepared MOF nanosheets could decrease the surface energy and then promote the formation of individual MOF nanosheets. For example, gluconate, a hydrophilic short-chain

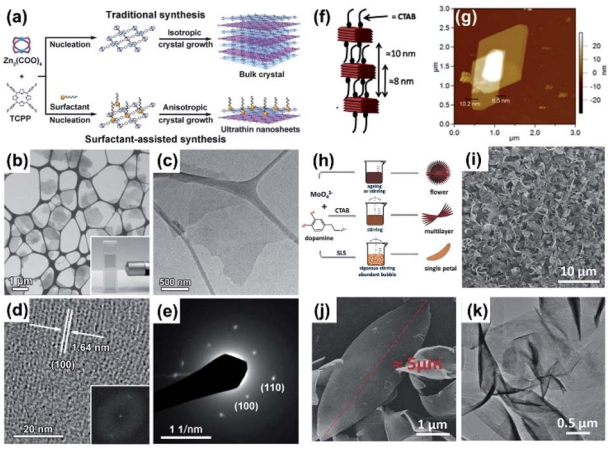

Fig. 10 PVP-assisted synthesis of Zn-TCPP nanosheets. (a) Schematic illustration of the traditional synthesis and surfactant-assisted synthesis of the Zn-TCPP MOF. (b) STEM image of Zn-TCPP nanosheets obtained by SEM with a transmission electron detector. Inset: Tyndall effect of colloidal Zn-TCPP nanosheets in ethanol. (c) TEM image of a single Zn-TCPP nanosheet. (d) HRTEM image of Zn-TCPP nanosheets and corresponding FFT pattern (inset). (e) SAED pattern of Zn-TCPP nanosheets in (c). CTAB-assisted synthesis of Zn-MOF nanosheets. Reproduced with permission.[86] Copyright©2015 WILEY-VCH Verlag GmbH & Co. KGaA. (f) Schematic illustration and (g) AFM images of the Zn-MOF nanosheets. Reproduced with permission.[66] Copyright©2013 American Chemical Society. CTAB and SLS assisted preparation of Mo–polydopamine nanosheets. (h) Schematic illustration, (i and j) SEM images, and (k) TEM image of Mo–polydopamine nanopetals. Reproduced with permission.[98] Copyright©2018 WILEY-VCH Verlag GmbH & Co. KGaA.

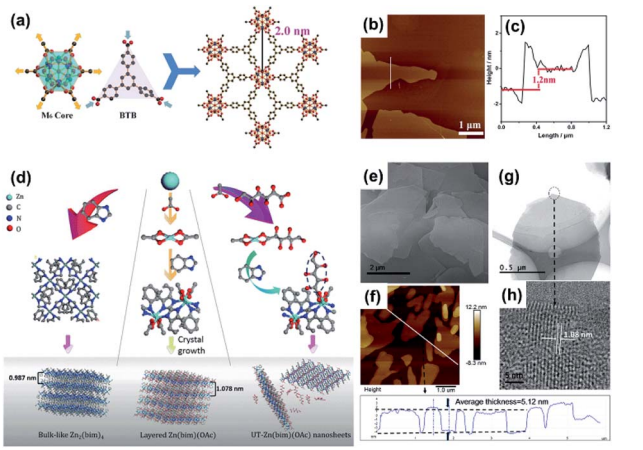

Fig. 11 (a) Schematic illustration, (b) AFM, and (c) height profile of $Hf_6(\mu_3\text{-}O)_4(\mu_3\text{-}OH)_4\text{-}(HCO_2)_6(BTB)_2$ MOF nanosheets. Reproduced with permission.[100] Copyright©2016 WILEY-VCH Verlag GmbH & Co. KGaA. (d) Schematic illustrations of the synthesis of $Zn_2(bim)_4$, Zn(bim)(OAc), and UT-Zn(bim)(OAc). (e) SEM, (f) AFM and height profile, (g) TEM, and (h) HRTEM images of UT-Zn(bim)(OAc). Reproduced with permission.[101] Copyright©2018 The Royal Society of Chemistry.

carboxylic acid that could pre-coordinate with Zn^{2+}, was used as the crystal growth inhibitor to synthesize ultrathin Zn(bim)(OAc) in a water/ethanol mixed solution. As shown in Fig. 11d, each layer of the 2D Zn(bim)(OAc) MOFs is constructed by two kinds of chains (*i.e.*, $Zn_2(bim)_4$ chains along the *b* axis and $Zn_2(OAc)_4$ chains along the *c* axis) cross-connected by Zn^{2+}.[101] During the reaction, gluconate partially replaced OAc^-, which could effectively break the interaction between the adjacent Zn(bim)(OAc) layers. The SEM (Fig. 11e), AFM (Fig. 11f), and TEM (Fig. 11g and h) images demonstrate the formation of the individual Zn(bim)(OAc) MOF nanosheets. The height profile measured from the AFM image implies that the Zn(bim)(OAc) nanosheets have an average thickness of about 5.12 nm. In addition, the yield of the 2D Zn(bim)(OAc) nanosheets is as high as 65% without forming any bulk MOF crystals, which provides a new approach to producing high-quality 2D MOFs. In addition to the gluconate, sucrose and pyridine[105] are also effective pre-coordination reagents for the molecule-pre-coordinated synthesis of 2D MOFs.

2.2.5. Other bottom-up methods. Although the surfactant-assisted and small molecule-precoordinated methods could enhance the yield and quality of the synthesized 2D MOFs, the metal centers of these 2D MOFs are largely blocked by the surfactants and small molecules, which hampers their applications in some fields such as catalysis. In this regard, the synthetic strategies without using the assistant molecules to achieve anisotropic growth of ultrathin MOF nanosheets, such as microfluidic fabrication, thermodynamic-controlled growth, and organic linker-controlled growth, have received gradually increasing attention.[106] Zhao and co-workers successfully fabricated 3 nm Zr-BTB nanosheets *via* a microdroplet flow reaction (Fig. 12a).[104] The dynamic mixing reactions, dominated by diffusion and forced convection in the microdroplet flow system, led to the anisotropic growth of 2D ZrBTB (MF-ZrBTB).[104] The TEM images and Tyndall light scattering effect of the as-fabricated MF-ZrBTB evidence its nanosheet nature and the AFM image with a height profile shows that the thickness of the MF-ZrBTB nanosheets is about 3.3 nm (Fig. 12b and c). In addition, tuning of the organic linkers to achieve the growth of the 2D MOFs and enhancing the interlayer distance by selecting large molecule linkers are possible solutions for the preparation of 2D MOF nanosheets without using the assistant molecules.[107] However, continuous efforts are needed in the preparation of high-quality 2D MOF nanosheets at a high yield.

2.2.6. Comparison of different synthetic strategies for 2D MOFs. Numerous efforts have been put into fabricating 2D MOF nanosheets with desirable properties. Herein, we summarize the advantages and disadvantages of these synthetic methods in order to provide clearer guidance for the future synthesis of 2D MOF nanosheets (Table 1). In general, the top-down approach requires layered MOFs as the precursors. The 2D MOF nanosheets exfoliated from the layered MOFs by using physical and chemical exfoliation usually have nonuniform thicknesses and morphologies due to the irregular forces in these methods. Nevertheless, the 2D MOF nanosheets prepared by using the top-down approach always possess abundant surface defects originating from the breakage of the interlayer interactions,

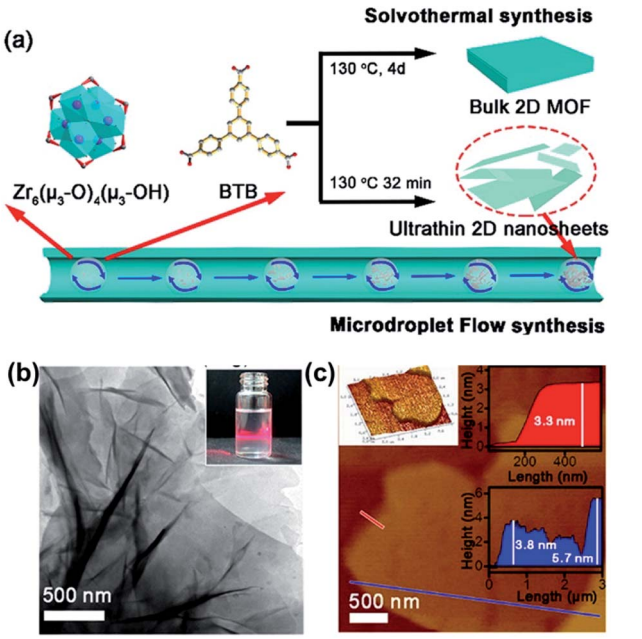

Fig. 12 (a) Schematic illustrations of the overall process developed to produce 2D MF-ZrBTB and ST-ZrBTB *via* microdroplet flow reaction and conventional solvothermal methods. (b) TEM image of MF-ZrBTB. The inset shows the Tyndall light scattering effect of MF-ZrBTB colloidal suspension. (c) AFM image and corresponding height profiles of MF-ZrBTB nanosheets along the red and blue lines. Reproduced with permission.[104] Copyright©2018 American Chemical Society.

which facilitates their applications in catalysis and sensors. In contrast, the bottom-up approach could fabricate the 2D MOF nanosheets with well controllable thicknesses and morphologies. The thickness and lateral size of the 2D MOFs can be well regulated by applying various reaction conditions or using different functional additives. Therefore, the bottom-up approach has drawn increasing attention to the production of high-yield and high-quality 2D MOF nanosheets. However, some of the drawbacks of the 2D MOF nanosheets produced by the bottom-up approach, *e.g.*, the coverage of the surface by the additional additives and poor structural stability, have hindered their direct use in surface-relative applications. Nevertheless, the 2D MOF nanosheets produced by the bottom-up approach show great potentials as precursors for MOF-derivatives due to their high yield and controllable thicknesses. To further guide the design of the 2D MOF nanosheets toward desirable applications, we then summarize the specific applications of 2D MOFs and their derivatives for electrochemical energy storage and electrocatalysis.

3. 2D MOFs for electrochemical energy storage and electrocatalysis

3.1. Application of 2D MOFs for energy storage

3.1.1. 2D MOFs for batteries. Batteries, especially lithium-ion batteries (LIBs), are the most valuable energy storage devices due to their high energy density and excellent stability.[108–110] The electrodes (*i.e.* the cathode and anode) where

Table 1 Comparison of the synthetic methods for 2D MOF nanosheets

	Top-down approach		Bottom-up approach				
Method	Physical exfoliation	Chemical/ electrochemical exfoliation	Template-assisted	Two-phase interfacial growth	Intermediate layer growth	Surfactant-assisted	Molecule-precoordination
Thickness	Thin	Thin	Medium	Thin	Medium	Ultrathin	Ultrathin
Uniformity	Low	Low	Good	Good	Good	Excellent	Excellent
Lateral size	Medium	Small	Medium	Large	Large	Small	Small
Condition	Mild	Mild	Harsh	Harsh	Harsh/medium	Medium	Medium
Yield	Medium	Medium	Low	Low	Medium	High	High
Defect	Abundant	Abundant	Low	Low	Low	Medium	Medium
Application	Gas separation	Catalysis	Gas adsorption, catalysis	Gas separation	Gas separation, photocatalysis	DNA detection, LIBs, catalysis, derivatives	Derivatives
Reference	22, 65, 69, 71 and 73	74, 75 and 77	84 and 87	76, 90, 91 and 94	96 and 97	86, 98 and 99	100 and 101

the electrochemical reactions occur are the key components in batteries. The electrochemical performance of the batteries significantly depends on the properties of the electrode materials, *e.g.*, the active surface area, conductivity, pore structure, and the number of redox-active sites.[111]

2D MOF nanosheets with a large content of Li^+ storage sites have been directly used as the anode materials in LIBs. For instance, porous [Mn(tfbdc)(4,4′-bpy)(H_2O)$_2$] (Mn-LCP) nanosheets were fabricated by mixing 2,3,5,6-tetrafluoroterephthalatic acid (H_2tfbdc), 4,4′-bipyridine (4,4′-bpy), and manganese(II) acetate tetrahydrate in D.I. water for five days. Based on the FT-IR, XPS, and magnetic studies, the lithium storage in the Mn-LCP nanosheets could be attributed to the substitution of the Mn(II) ions for Li^+.[112] However, the structure destruction of the Mn-LCP nanosheets caused by the Li^+ substitution led to a quite poor cycling performance (with a capacity retention of 76.6% after 50 cycles) and low first-cycle coulombic efficiency (31.5%). Similar to the Mn-LCP, a hierarchical tremella-like 2D Al-MOF (aluminum fumarate), fabricated using $Al(NO_3)_3 \cdot 9H_2O$ and $AlCl_3 \cdot 6H_2O$, exhibited a specific capacity of 392 mA h g^{-1} after 100 cycles at 37.5 mA g^{-1}.[113] Obviously, the capacity of these MOF nanosheets as the LIB anodes arises from the redox reaction of the metal sites, which causes serious structural destruction and low stability of these MOF anodes. Thus, employing more nonstructural sites for Li^+ storage should enhance the stability and capacity of the MOF anodes. To date, two simple methods have been employed to modify 2D MOF-based LIB anodes. One is the intercalation of the metal ions (*e.g.*, Fe^{III} ions) with variable valences into the MOFs, which could greatly enhance the specific capacity of the MOF-based electrode materials.[114] Besides these metal centers as the active sites, some of the uncoordinated ligands could also undergo redox reactions to store the lithium ions. Li and coworkers synthesized manganese-based ultrathin MOF nanosheets (Mn-UMOFNs) from BDC and $MnCl_2$ *via* an ingenious ultrasonication route (Fig. 13a).[115] Mn-UMOFNs with thicknesses of 1.8–7.0 nm (mostly <3 nm) (Fig. 13b) showed a high capacity (1187 mA h g^{-1} at 100 mA g^{-1} for 100 cycles) and ultrahigh rate performance (701 mA h g^{-1} at 2 A g^{-1}) (Fig. 13c). The excellent rate performance of the Mn-UMOFNs could be attributed to their ultrathin morphology which could greatly enhance the diffusion of Li^+. The high capacity was attributed to the two-step lithium intercalation on the Mn-UMOFNs, *i.e.* the first step involved a reduction process of Mn^{2+} to Mn^0 (at above 0.5 V) and the second step involved a process at a low voltage (below 0.5 V) in which the coordinated oxygen atoms with high electronic density as well as the benzene rings with delocalized π electrons work as the active sites for lithium intercalation (Fig. 13d). However, most of the synthesized 2D MOFs have a relatively low conductivity and therefore cannot meet the requirements of the high-rate charge–discharge. Coupling the 2D MOFs with conductive substrates could alleviate this problem. Jin and co-workers reported a hybrid material of 2D NiCo-MOFs and black phosphorus (BP).[116] The bulk BP was firstly exfoliated to few-layer BP nanosheets. Then the few-layer BP nanosheets were directly added into the mixed solution of Co^{2+}, Ni^{2+}, and BDC (Fig. 13e). After continuous sonication in an ice bath for 8 h, BP/NiCo-MOFs were successfully obtained. The SEM (Fig. 13f) and TEM images (Fig. 13g and h) demonstrate that this BP/NiCo MOF hybrid has a nanosheet morphology with a thickness of ~6 nm. The EDS mapping analysis (Fig. 13i) of the BP/NiCo-MOF hybrid nanosheets evidences that the NiCo-MOFs uniformly form a cover on the BP nanosheets. The synthesized BP/NiCo-MOF nanosheets exhibited a high discharge capacity of about 2483 mA h g^{-1} at 0.1 mA g^{-1} in the first cycle and a high reversible capacity (853 mA h g^{-1}) at 0.5 A g^{-1} (Fig. 13j). Moreover, the hybrid 2D MOFs also exhibited excellent rate performance (with a high reversible capacity of 436 mA h g^{-1} at 5 A g^{-1}) and high capacity retention of 398 mA h g^{-1} after 1000 cycles at the charge–discharge current density of 5 A g^{-1} (Fig. 13k). The superior electrochemical performance of the BP/NiCo-MOF hybrid nanosheets can be ascribed to the synergistic effects of the few-layer BP and NiCo-MOF nanosheets, *i.e.*, BP and NiCo-MOF both provide sufficient redox-active sites, while the few-layer structure and high conductivity

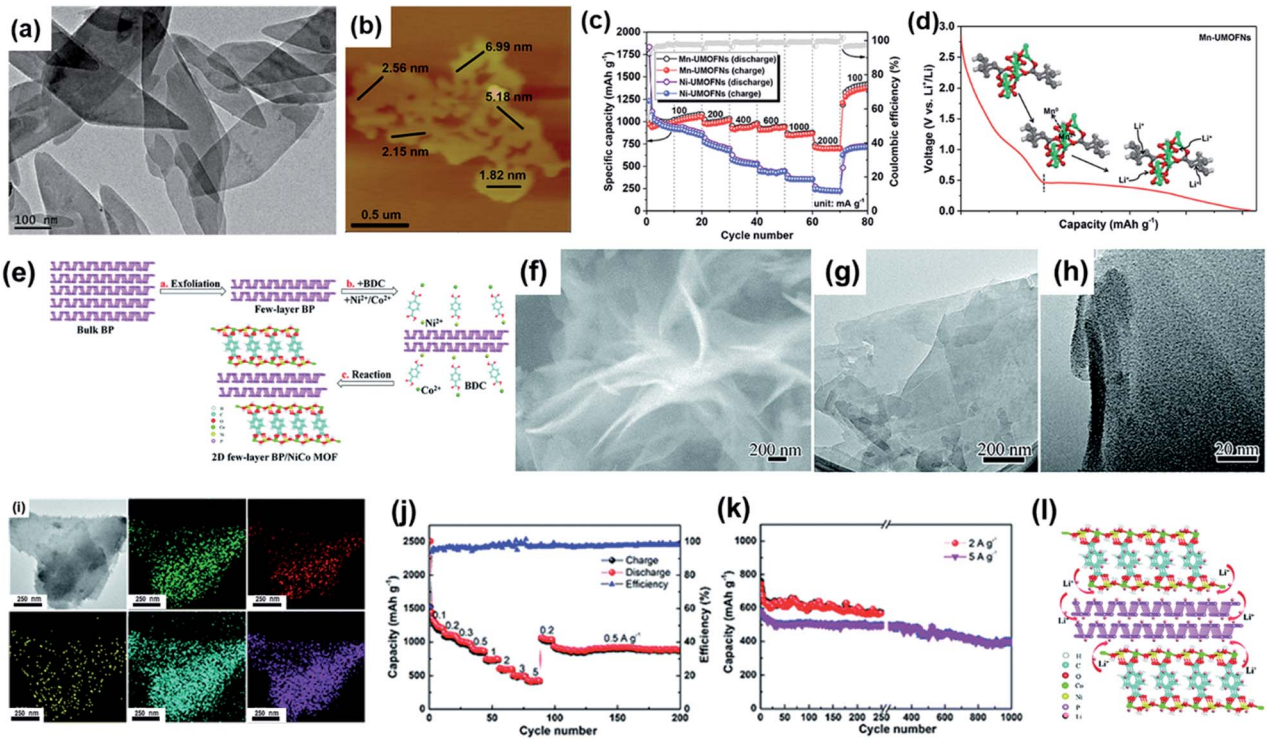

Fig. 13 (a) TEM and (b) AFM images of Mn-UMOFNs. (c) Rate performance of Mn-UMOFNs and Ni-UMOFNs at various current densities from 100 to 2000 mA g^{-1}. (d) Proposed electrochemical redox action mechanism of Mn-UMOFNs. Reproduced with permission.[115] Copyright©2017 American Chemical Society. (e) Illustration of the preparation process of the 2D BP/NiCo MOF hybrid. (f) SEM image, (g and h) TEM images, (i) EDS mapping, (j) rate performance, (k) cycle performance, and (l) illustration of the Li^+ insertion of the BP/NiCo MOF NSs. Reproduced with permission.[116] Copyright©2019 The Royal Society of Chemistry.

of the BP provide short diffusion paths and fast electron-charge transfer.

3.1.2. 2D MOFs for supercapacitors (SCs). Compared to batteries, SCs possess higher power densities and can tolerate larger charge–discharge current densities.[117] According to the energy storage mechanism, the SCs could be divided into two types, *i.e.*, the electrical double layer capacitors (EDLCs) and pseudo-capacitors. A high-performance SC electrode should own a high active surface area and provide sufficient channels for the rapid diffusion of ions. Thus, 2D MOF nanosheets with a high accessible surface area, abundant pore structure, and redox metal centers have been widely explored as the electrode materials for SCs. For instance, the Co-BDC nanosheet electrode achieved a high capacitance of 1159 F g^{-1} at a current density of 0.5 A g^{-1}.[120] More importantly, this electrode exhibited high capacitance retention of 96.7% after 6000 cycles at the current density of 2 A g^{-1}, indicating the high stability of the Co-BDC nanosheets as the SC electrode materials. Further investigations implied that the capacitance of the Co-BDC nanosheets was mainly due to the redox reactions between Co(II)/Co(III)/Co(IV), which can be expressed as follows:

$$\text{Co(II)–L} + \text{OH}^- = \text{Co(III)(OH)–L} + \text{e}^- \quad (1)$$

$$\text{Co(III)(OH)–L} + \text{OH}^- = \text{Co(IV)–O–L} + \text{H}_2\text{O} + \text{e}^- \quad (2)$$

where L represents the ligand (BDC).

In addition, Abazari and coauthors reported a fast and simple technique to synthesize S^{2-}-modified layered MOF nanosheets ([Co(4,4′-oxybis(benzoic acid))$_2$(*N*,*N*′-bis-(4-

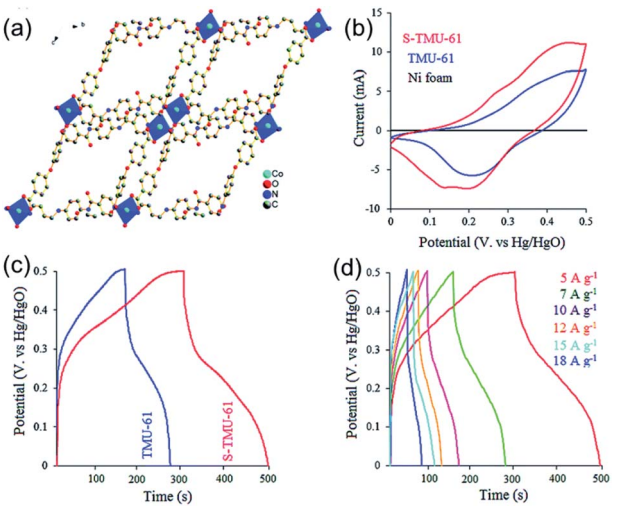

Fig. 14 (a) Topological diagram of TMU-61. (b) CV curves of TMU-61, S-TMU-61, and Ni foam at a scan rate of 25 mV s^{-1}, (c) GCD curves of TMU-61 and S-TMU-61 electrode materials at a current density of 5 A g^{-1} and (d) GCD curves of S-TMU-61 at different current densities. Reproduced with permission.[118] Copyright©2019 The Royal Society of Chemistry.

pyridylformamide)-1,4-benzenediamine)$_4$](DMF)$_2$, S-TMU-61) (Fig. 14a),[118] which could also be employed as the SC electrode material and exhibited an ultrahigh capacitance of 636.6 F g^{-1} at 5 A g^{-1} (Fig. 14b–d). The asymmetric SC (ASC) assembled by using S-TMU-61 as the electrode material showed a high energy density (25.73 W h kg^{-1}) and power density (2549.3 W kg^{-1}). The capacitance of these kinds of MOFs was mainly attributed to the pseudo-capacitance of the redox reaction of the metal centers. Therefore, the number of active sites for the charge storage and the conductivity of the 2D MOFs are essential for their capacitance and rate performance, which are still challenges in the development of 2D MOF-based SCs.

Conductive MOFs, a series of conjugated planar polymers, are considered as the next-generation energy storage materials due to the combined advantages of MOFs and conductive materials. Their active sites and structural properties could be flexibly adjusted to match the requirements of different types of energy storage devices. The Bao group designed two kinds of conductive 2D MOFs (Fig. 15a), *i.e.*, M-HAB (M = Cu, Ni, and Co; HAB = hexaaminobenzene) and Cu-HHB (HHB = hexahydroxybenzene).[119,121,122] Among them, conductive M-HABs with redox-active sites were investigated as the electrode materials of SCs. The HRTEM and HAADF-STEM images of the as-prepared Cu-HAB clearly show pores smaller than 1 nm with a honeycomb arrangement along the [001] direction with d_{100} = 1.15

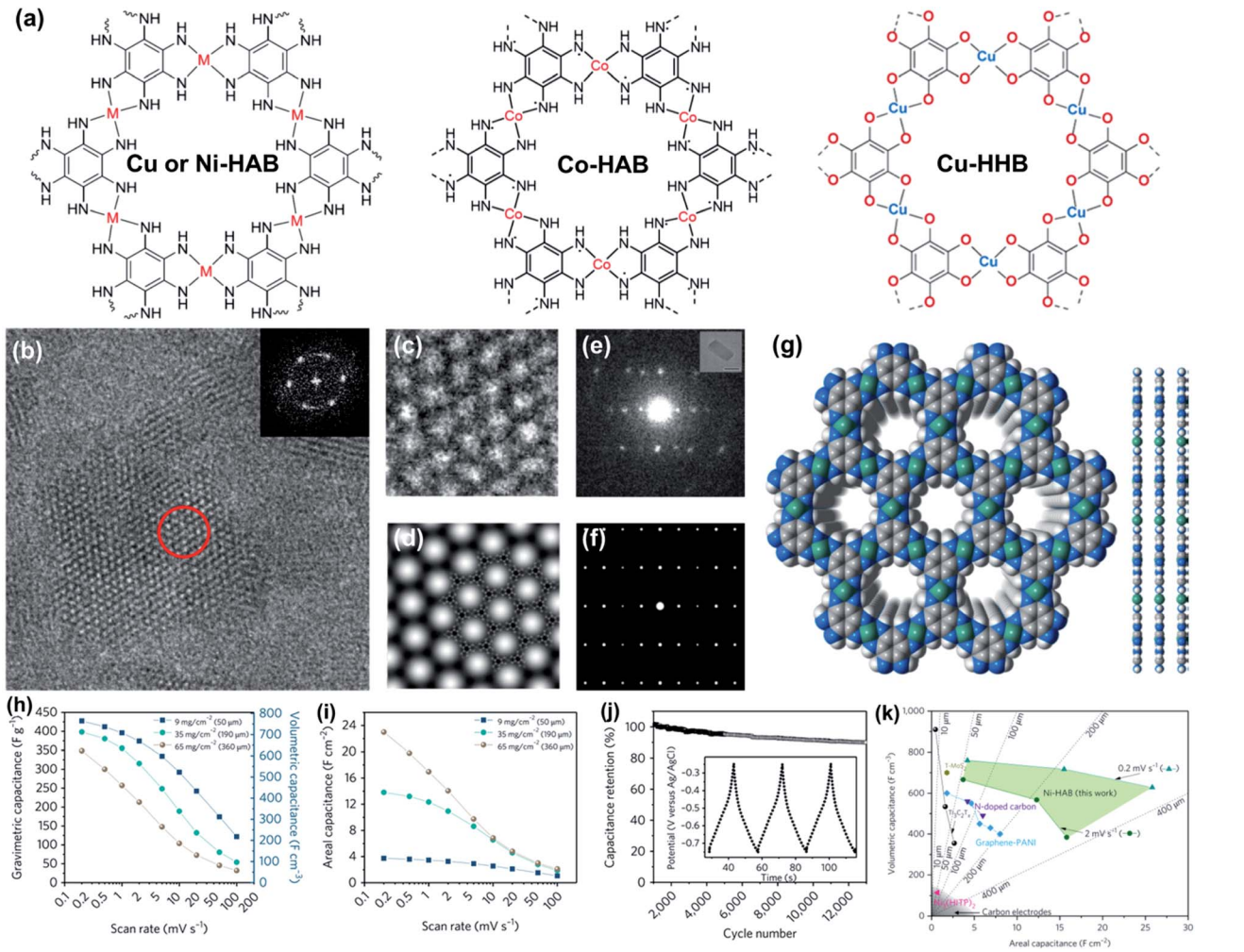

Fig. 15 (a) 2D MOFs in $M_3(C_6X_6)_2$ (M = Cu, Co, and Ni. X = NH, S, and O) family. (b) HR-TEM image of Cu-HAB along [001] that shows a hexagonal pore packing with *d* 100 = 1.15 nm (*a* = 1.33 nm). Scale bar, 10 nm. Inset: Fourier transform of the image. (c) HR-TEM image of the region within the red circle in (b). (d) Symmetry-imposed and lattice-averaged image calculated from the HR-TEM image. Embedded is the eclipsed structure model of Cu-HAB. Scale bar, 2 nm. Experimental (e) and simulated (f) electron-diffraction pattern (eclipsed model) of Cu-HAB viewed along [−110]. Scale bar 5 nm^{-1}. Inset (e): the crystal from which the electron-diffraction pattern was taken. Scale bar, 50 nm. (g) A space-filling model of the Cu-HAB model. Blue, grey, green and white spheres represent N, C, Ni and H atoms, respectively; a.u.: arbitrary units. (h) Gravimetric and volumetric rate performance for Ni-HAB pellet electrodes with different areal densities of 9, 35, and 65 mg cm^{-2}. (i) Areal rate performance for the Ni-HAB electrodes with different weight loadings. (j) Capacitance retention data collected by galvanostatic charge–discharge at 10 A g^{-1}. Inset: galvanostatic charge–discharge profiles. (k) Comparison of the volumetric and areal capacitances of Ni-HAB additive-free electrodes (green area) with the performance of other materials. Reproduced with permission.[119] Copyright©2018 Nature Publishing Group.

nm (Fig. 15b–g). Since the HAB linkers prefer to coordinate with d^8 and d^9 metal species with a square-planar coordination geometry, which could well maintain the highly ordered pore channels along the (001) direction, M-HABs display excellent diffusion ability as the SC electrode. Ni-HAB and Cu-HAB exhibited high gravimetric capacitances of 420 F g^{-1} and 215 F g^{-1} at the scan rate of 0.2 mV s^{-1}, respectively (Fig. 15h). The higher capacitance of Ni-HAB could be attributed to the oxidation of Ni(II) to a higher valence state (Ni(IV)), which possessed a larger pseudocapacitance compared to Cu-HAB. Another important advantage of the Ni-HAB electrode was that the assembled 2D conductive MOF sample had a high volumetric density of 1.8 g cm^{-3}, which led to a volumetric capacitance as high as 760 F cm^{-3} (Fig. 15h) and an areal capacitance of 22.5 F cm^{-2} at 0.2 mV s^{-1}. This volumetric capacitance is abnormally high for the electrode with a thickness of 50 μm and almost surpasses the best values of the carbon electrodes reported for SCs (Fig. 15k).[1,5,123,124] Ni-HAB also possessed high stability with capacitance retention of 90% after 12 000 cycles at the charge–discharge current density of 10 A g^{-1} (Fig. 15j). Besides these hexasubstituted benzene based conductive MOFs, 2D Ni_3(-HITP)$_2$ (HITP = 2,3,6,7,10,11-hexaiminotriphenylene) with a remarkable bulk conductivity (5000 S m^{-1}) has also exhibited excellent capacitive performance with a capacitance of 111 F g^{-1} at 0.05 A g^{-1} and 90% capacitance retention after 10 000 cycles at a current density of 2 A g^{-1}.[125]

3.2. Applications of 2D MOFs in electrocatalysis

The electrochemical catalytic reactions are types of surface reactions, in which the catalytic performance of the catalysts greatly depends on their surface properties. 2D MOFs, with the advantages of high active surface areas and flexible surface chemical compositions, are regarded as promising catalysts. Although the poor stability and low conductivity of some easily prepared 2D MOFs have limited their applications in electrocatalysis, recent work has demonstrated that the applications of the 2D MOFs as the electrocatalysts for the OER, ORR, HER, and CO_2RR could be realized by constructing 2D MOFs/conductive substrate composites or by using conductive 2D MOFs.

3.2.1. 2D MOFs for the OER. Similar to the transition metal (Fe, Co, Ni, Mn) oxide/hydroxide/oxyhydroxide based high-performance OER electrocatalysts,[126–130] MOFs containing transition metal ions could also exhibit high catalytic performance toward the OER (Table 2). The Pang group synthesized ultrathin 2D $Co_2(OH)_2$(BDC) nanosheets with a thickness of ~2 nm by a simple surfactant-assisted hydrothermal method, which exhibited good electrocatalytic activity for the OER with a low overpotential of 263 mV at 10 mA cm^{-2}, a Tafel slope of 74 mV dec^{-1}, and good stability (~5% degradation for 4 h at 1.5 V *vs.* RHE) in 1.0 M KOH.[131] The authors claimed that the high OER performance should be ascribed to the large amount of unsaturated Co^{II} active centers on the surface of the $Co_2(OH)_2$(BDC) nanosheets which could convert to highly active Co^{IV}–OH intermediate sites.[127] In addition, bimetallic 2D MOFs, such as Ni/Co MOF nanosheets, have displayed much better catalytic OER performance compared to the corresponding single-metallic 2D MOFs.[132–134] For instance, the Tang group reported ultrathin bimetallic Ni/Co MOF nanosheets (NiCo-UMOFNs) with a thickness of about 3.1 nm (Fig. 16a–d).[134] These NiCo-UMOFNs presented a low overpotential of 250 mV at the current density of 10 mA cm^{-2} with a small Tafel slope of 42 mV dec^{-1} and excellent stability while being used as an OER electrocatalyst under alkaline conditions (Fig. 16e and f). The superior performance of the NiCo-UMOFNs could be attributed to the orderly distributed metal atoms in the NiCo-UMOFNs (as shown in the HAADF-STEM image in Fig. 16c), which could provide sufficiently exposed active sites for the OER. Moreover, the authors evidenced that the coupling effect between Co^{2+} and Ni^{2+} in NiCo-UMOFNs (*i.e.*, a part of the electrons have

Table 2 Comparison of the OER and HER performances of different 2D MOFs

Material/substrate	Application	Loading (mg cm^{-2})	Electrolyte	η (mV) @ 10 mA cm^{-2}	Tafel slope (mV dec^{-1})	Catalytic stability	Ref.
$Co_2(OH)_2$BDC/GC	OER	0.25	1 M KOH	263	74	~5% degradation for 4 h at 1.5 V	131
NiCo-UMOFNs/GC	OER	0.2	1 M KOH	250	42	Almost unchanged for 3 h at 1.5 V	134
Ni-MOF@Fe-MOF/GC	OER	0.2	1 M KOH	265	54	N/A	138
NiFe-UMNs/GC	OER	0.4	1 M KOH	260	30	Almost unchanged for 3 h at 1.5 V	139
Co-ZIF9/GC	OER	0.21	1 M KOH	380	55	~6% degradation for 10 h at 1.7 V	140
MOF/OM-NFH/GC	OER	0.4	1 M KOH	270	123	~18% degradation for 11 h at 1.5 V	132
MIL-53(FeNi)/NF	OER	N/A	1 M KOH	233 @ 50 mA cm^{-2}	31.3	Almost unchanged for 4 h at 1.45 V	133
$NiFe_{0.2}Co_{0.3}$-ZIF/NF	OER	N/A	1 M KOH	216 @ 100 mA cm^{-2}	23.25	Almost unchanged for 20 h at 1.52 V	141
Co-BTH/GC	HER	N/A	H_2SO_4 (pH = 1.3)	185	88	N/A	142
Ni-THT/GC	HER	N/A	0.5 M H_2SO_4	330	80.5	N/A	143
Co-THTA	HER	N/A	0.5 M H_2SO_4	283	74	Unchanged for 4 h at 10 mA cm^{-2}	144
UiO-66-NH_2-Mo/GC	HER	N/A	0.5 M H_2SO_4	125	59	Almost unchanged for 7 h at −0.2 V	145
$Ni_{0.8}Fe_{0.2}$-MOF/NF	OER	N/A	0.1 M KOH	240	34	~3% degradation for 5.5 h at 1.42 V	146
	HER			134	N/A	Almost unchanged for 5.5 h at −0.2 V	
NiFeZn-MNS/NF	OER	N/A	1 M KOH	308 @ 50 mA cm^{-2}	49	~5% degradation for 120 h at 1.62 V	147
	HER			180	N/A	N/A	
IrO_2	OER	N/A	0.5 M KOH	411	91	N/A	148
RuO_2	OER	N/A	0.5 M KOH	358	55	N/A	148

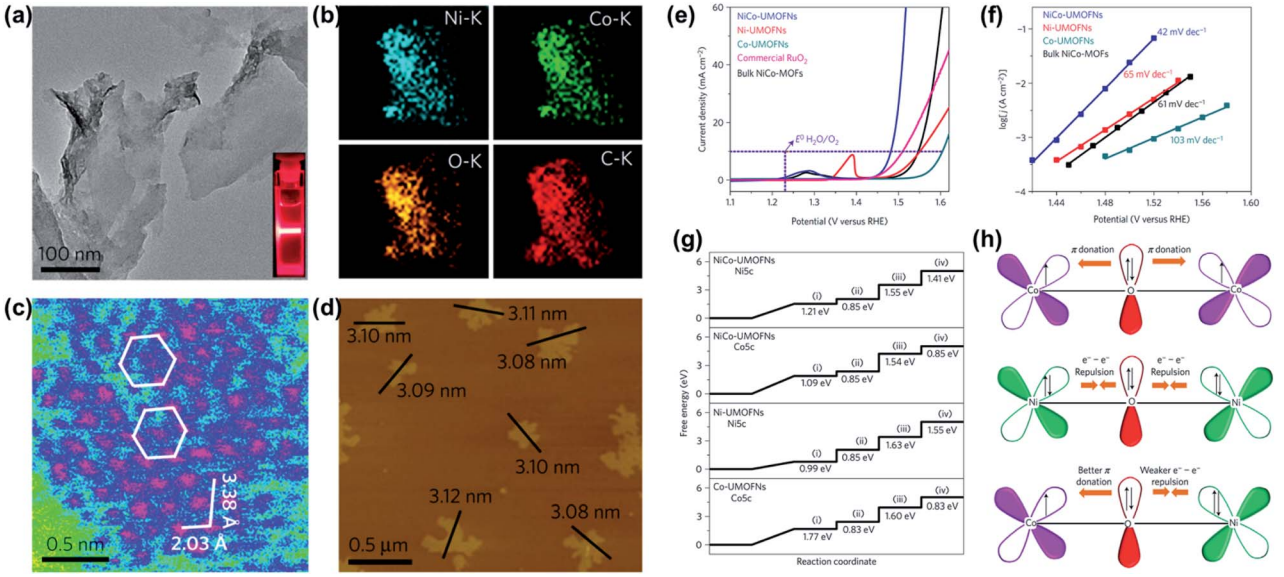

Fig. 16 (a) TEM image of NiCo-UMOFNs. The inset shows the Tyndall light scattering of NiCo-UMOFNs in an aqueous solution. (b) TEM-EDS mapping images of NiCo-UMOFNs. (c) HAADF-STEM image of the (200) plane for NiCo-UMOFNs showing the hexagonal arrangement of the metal atoms. The pink colour represents metal atoms, blue is for light elements (carbon and oxygen), and green is for the background. (d) AFM image of as-prepared NiCo-UMOFNs, showing measured dimensions of individual flakes. (e) Polarization curves of NiCo-UMOFNs, Ni-UMOFNs, Co-UMOFNs, RuO_2 and bulk NiCo-MOFs in O_2-saturated 1 M KOH solution at a scan rate of 5 mV s^{-1}. (f) Tafel plots of NiCo-UMOFNs, Ni-UMOFNs, Co-UMOFNs and bulk NiCo-MOFs derived from Koutecky–Levich plots in O_2-saturated 1 M KOH solution. (g) Standard free energy diagram of the OER process on UMOFNs surfaces. (h) Schematic representation of the electronic coupling between Co and Ni in UMOFNs. Reproduced with permission.[134] Copyright©2016 Nature Publishing Group.

transferred from Ni^{2+} to Co^{2+} through the oxygen of the ligands) and the coordinatively unsaturated metal sites on the surface were constructive for the high electrocatalytic performance of NiCo-UMOFNs toward the OER. As shown in Fig. 16g and h, the electron transferred from Ni^{2+} to Co^{2+} could strengthen the π-donation of the Co^{2+} sites and weaken the e^-–e^- repulsion of the Ni^{2+} sites, both of which could enhance the electron-withdrawing ability of NiCo-UMOFNs and consequently lower the OER overpotential. Similar to the NiCo-UMOFNs, some other 2D bimetallic MOFs, such as Fe/Ni-MOFs,[135] Fe/Co-MOFs,[136] and Co–Fe/Ni@HPA-MOF,[137] also exhibited excellent catalytic performance for the OER.

3.2.2. ORR. Commercial fuel cells demand precious metal catalysts to boost the ORR on the cathodes. The development of highly efficient ORR electrocatalysts at low costs is urgently needed. Low-cost electrocatalysts, such as non-precious transition metal oxides,[149] carbon materials,[150,151] and non-precious metal–nitrogen–carbon composites,[152] are widely employed as the electrocatalysts for the ORR. Usually, pure MOFs with low stability, high-valance metal centers, and poor conductivity are not suitable for the ORR application. Although various MOFs, such as $[Cu_2(OH)(bpy)_2(btc)_3]$, $[Fe_2(Fe(tcpp))Cl]$, $[Cu_3(btc)_2(H_2O)_3]$, and $[Co(mim)_2]$, have been employed as the ORR electrocatalysts,[153–157] the conductivity of these 2D MOFs still cannot meet the high requirements for the high-performance ORR electrocatalysts and the half-wave potential ($E_{1/2}$) of the ORR on these 2D MOFs is always lower than 0.80 V *vs.* RHE (V_{RHE}). Compositing active 2D MOFs with conductive substances could effectively enhance the overall conductivity of the resulting hybrid materials. For example, copper-centered MOF nanosheets composited with graphene achieved a much better catalytic performance toward the ORR.[158] However, the greatest challenge for conventional 2D MOFs as the electrocatalysts is to break the electrical blockage on the metal centers driven from the organic ligands.

Recently, several highly stable conductive 2D MOFs were also employed to catalyze the ORR. As shown in Fig. 17a–c, 2D $Ni_3(HITP)_2$ with a highly conjugated framework and a striking conductivity was used as the electrocatalyst for the ORR and exhibited an onset potential of 0.82 V_{RHE}.[159] More recently, Feng and coworkers prepared a series of conjugated MOFs and employed them as the ORR electrocatalysts. For example, a phthalocyanine-based layered 2D conjugated MOF was constructed using copper phthalocyanine (PcCu) and square-planar cobalt bis(dihydroxy) complexes (Co–O_4) as the linkages (PcCu–O_8–Co).[160] Fig. 17d displays the structure of PcCu–O_8–Co, which was periodically assembled using Co–O_4 and PcCu–O_4 coordination units. In this kind of MOFs, the square-planar Co–O_4 could not only efficiently transfer the electrons between the two conjugated PcCu to construct a large 2D conjugated plane but also work as highly active sites for the ORR due to its specific electronic configuration (with single-electron occupied e_g orbitals). Then, the PcCu–O_8–Co was composited with CNTs and exhibited further enhanced catalytic performance for the ORR with a $E_{1/2}$ of 0.83 V_{RHE} and a limiting current density of 5.3 mA cm^{-2} (Fig. 17e). This work for the first time highlighted 2D MOFs as ORR electrocatalysts and verified that tuning the

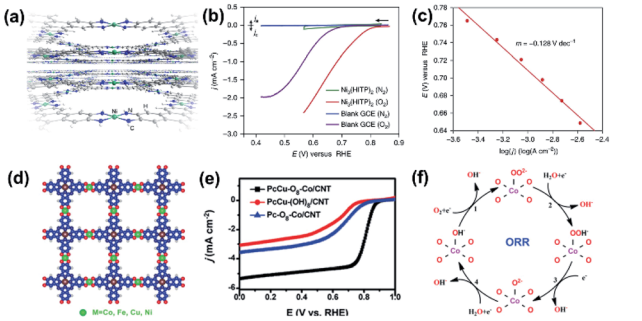

Fig. 17 (a) Perspective view of the 2D layered structure of $Ni_3(HITP)_2$. (b) Polarization curves of $Ni_3(HITP)_2$ in a N_2 (green) *versus* O_2 atmosphere (red) as well as of the blank glassy carbon electrode in a N_2 *versus* O_2 atmosphere (blue and purple, respectively). (c) Activation-controlled Tafel plot for the $Ni_3(HITP)_2$-electrocatalyzed ORR. Reproduced with permission.[159] Copyright©2016 Nature Publishing Group. (d) Structure of PcM-O_8-Co. (e) LSV curves for the as-prepared PcCu–O_8–Co/CNTs. (f) Possible reaction route for the ORR in CoO_4 sites. Reproduced with permission.[160] Copyright©2019 WILEY-VCH Verlag GmbH & Co. KGaA.

electronic structures of the 2D MOFs was an effective way to optimize their catalytic activities toward the ORR (Fig. 17f).

3.2.3. 2D MOFs for the HER. Hydrogen energy has been considered as a promising alternative to fossil fuels in the future energy strategies because it's environmentally friendly and renewable.[161] 2D transition metal-based (*e.g.* Fe, Co, and Ni) MOFs have been used (as alternatives to noble metal-based electrocatalysts) for catalyzing the HER during water electrolysis to increase the faradaic efficiency and lower the reaction overpotential.[162] Due to the advantage of well-dispersed metal active sites, metal (*e.g.*, Fe, Co, and Ni) dithiolene complexes are widely considered as one of the most efficient HER catalysts (Table 2). Marinescu *et al.* constructed 2D Co-based MOFs (Fig. 18a and b) with benzenehexathiol (BHT) or triphenylene-2,3,6,7,10,11-hexathiol (THT) as the organic linker to integrate the cobalt dithiolene catalytic sites.[162] Owing to the high Co loading and good stability, Co-BHT and Co-THT exhibited remarkable stability and catalytic activities with overpotentials of about 0.34 and 0.53 V at 10 mA cm^{-2}, respectively, under acidic conditions. With a higher average concentration of Co on the surface of Co-BHT, consequently, Co-BHT (3.7×10^{-6} mol_{Co} cm^{-2}) displayed better catalytic activity than Co-THT (2.5×10^{-6} mol_{Co} cm^{-2}). The authors also investigated 2D metal-BHT frameworks with different metal centers as the electrocatalysts for the HER at pH = 1.3.[142] The electrocatalytic activity of the investigated 2D metal-BHT frameworks followed the order of Co-BHT > Ni-BHT > Fe-BHT. In detail, Co-BHT showed the lowest HER overpotential of 185 mV at 10 mA cm^{-2}.[163] Apart from altering the kind of active metal centers in the 2D MOFs, improving the electronic structure (*e.g.* increasing the electronic density) of the metal sites is also an effective way to enhance the HER activity of 2D MOFs. Feng *et al.* immobilized three different metal sites, including metal dithiolene–diamine (MS_2N_2, M = Co and Ni), metal bis(dithiolene) (MS_4), and metal bis(diamine) (MN_4), into the 2D MOFs based on the metal dithiolene–diamine coordination (THTA-M), as shown in Fig. 18c.[144] The electrocatalytic HER activity of these 2D MOF-based catalysts followed the order of MS_2N_2 > MN_4 > MS_4. Particularly, for the THTA-Co integrated with MS_2N_2, the electrocatalytic H_2 evolution occurred at an overpotential of 283 mV at 10 mA cm^{-2} in 0.5 M H_2SO_4 (Fig. 18d). The theoretical calculations (Fig. 18e) demonstrated that, for proton reduction, the M–N units were more active than the other possible active sites (*e.g.*, N–N, N–S, –Co, Co–S, and S–S). Additionally, the coordination with S improved the H_2 adsorption ability of the atomic Co, leading to an enhanced HER catalytic activity of CoS_2N_2 compared to CoN_4 and CoS_4. Furthermore, bimetal-based MOFs also presented excellent catalytic performance for the HER. Zhao *et al.* reported a general dissolution–crystallization approach for the *in situ* growth of ultrathin nanosheet arrays of 2D bimetal-based MOFs.[146] The synthesized NiFe-MOFs demonstrated superior electrocatalytic performance toward the HER with good stability and a low overpotential of 134 mV at 10 mA cm^{-2} in 0.1 M KOH. The authors attributed such an outstanding HER activity to the optimal structural characteristics of the electrocatalysts, including highly exposed molecular metal active sites owing to the ultrathin MOF nanosheets, improved electrical conductivity through the 2D nanostructuration, and a combination of the hierarchical porosity.

3.2.4. 2D MOFs for the CO_2RR. 2D MOF-based catalysts without noble metal centers used for the CO_2RR have caught much attention due to their advantages in both molecular and geometric structures,[164–168] including the flexible manipulation of spatial arrangement of the active centers, the functionalized modification of linkers in frameworks, and the ultrathin morphology.[42] Yang *et al.* constructed the cobalt-porphyrin MOF, $Al_2(OH)_2$TCPP-Co, into a thin film on conductive substrates *via* atomic layer deposition.[169] Compared to other metal-centered (*e.g.* Zn and Cu) porphyrins, $Al_2(OH)_2$TCPP-Co revealed the best CO selectivity with a faradaic efficiency of 76% at −0.7 V_{RHE} and excellent stability over 7 h with a turnover number (TON) of 1400. The authors attributed such an outstanding activity to the existence of Co(I) during the catalysis, where the CO_2 was bonded. For most MOF-based electrocatalysts for the CO_2RR, CO is the main product and multi-electron reduction products such as methane, ethanol, and ethylene barely appear. However, Koper *et al.* reported that Co protoporphyrin (CoPP) could not only reduce CO_2 to CO but also produce methane and a small amount of HCOOH and methanol.[170] The authors investigated the mechanism of CO_2RR on CoPP and revealed that the moderately acidic conditions were beneficial for the further reduction of CO due to the weak bonding of CO on Co(I). In that case, functionally modifying the linkers of the 2D MOFs would be an effective way to enhance the selectivity toward hydrocarbons or alcohols by strengthening the adsorption of the $*C_xH_yO_z$ intermediates, *e.g.* *CHO and *COCOH (the symbol "*" represents the adsorbed site), during the CO_2RR.

3.2.5. Challenges of 2D MOFs for electrocatalysis. 2D MOFs have been used as electrocatalysts not only due to their structural flexibility, but also due to their ultrathin morphology to expose the well dispersed metal centers to the maximum extent.

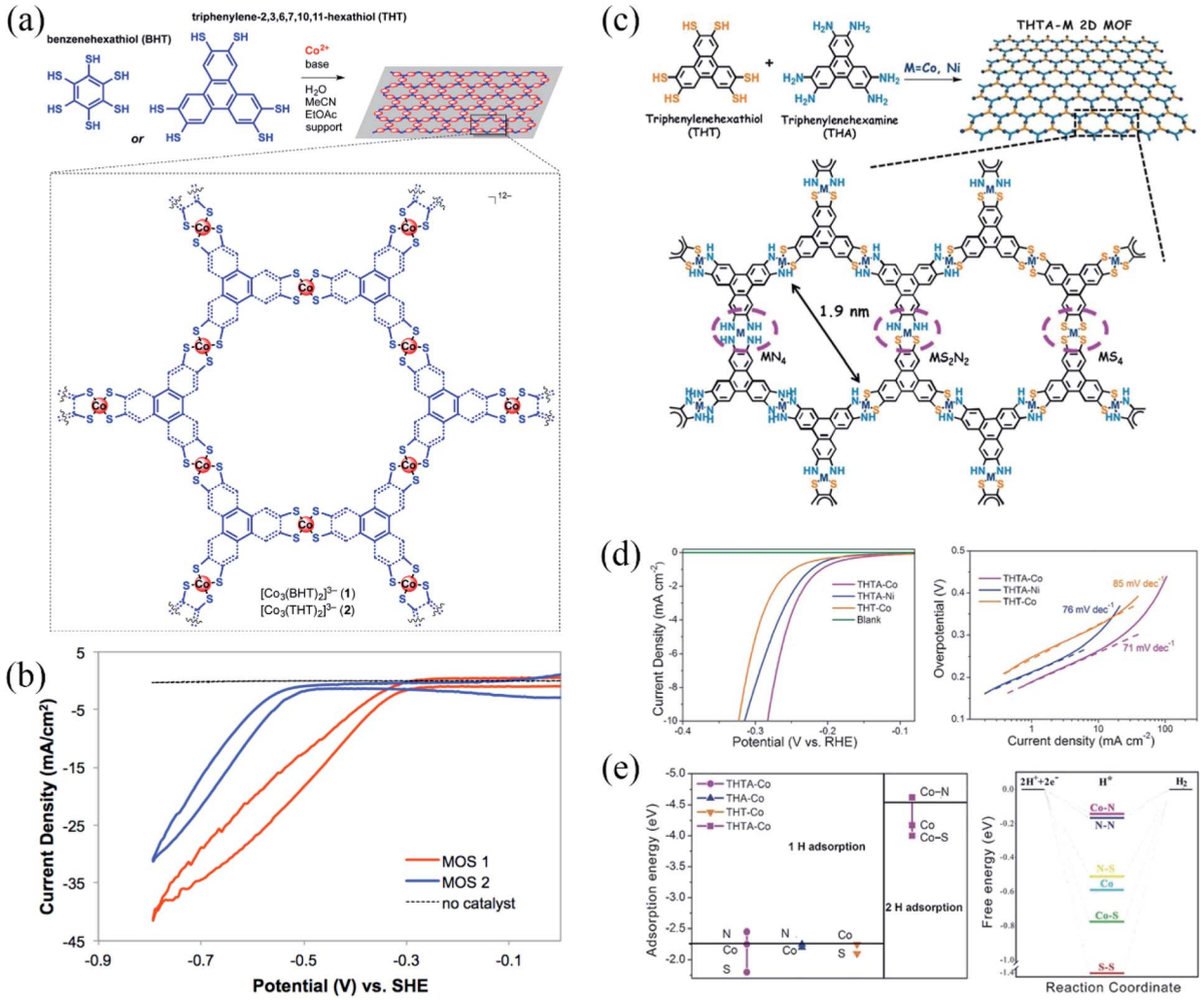

Fig. 18 (a) Synthesis of cobalt dithiolene films, Co-BHT and Co-THT, the films are deposited onto the desired supports, generating MOS_1 and MOS_2; (b) polarization curves of MOS_1 (red) and MOS_2 (blue) at pH 1.3, scan rate, 100 mV s^{-1}; reproduced with permission.[162] Copyright©2015 American Chemical Society. (c) The synthesis of single-layer 2D MOFs, in which MS_2N_2 complexes along with MN_4 and MS_4 moieties were incorporated into the hexagonal networks through metal dithiolene–diamine coordination (THTAM) (M = Co and Ni); (d) HER polarization plots (left) of three types of 2D MOFs: THTA-Co (purple), THTA-Ni (blue), and THT-Co (yellow) and a blank glassy carbon disk electrode in 0.5 M H_2SO_4 and the Tafel plots (right) obtained from the polarization curves; (e) the adsorption energy of one H and two H radicals bonding to the proposed active sites on the surface of THTA-Co, THA-Co, and THT-Co 2D MOFs (left) and the free-energy diagram of the HER at the equilibrium potential for the THTA-Co 2D MOFs with the possible active sites (right). Reproduced with permission.[144] Copyright©2017 WILEY-VCH Verlag GmbH & Co. KGaA.

Their catalytic activity could be enhanced *via* adjusting the electronic structure of the metal centers, such as generating unsaturated metallic active centers or increasing the electronic density of the active centers to strengthen the adsorption of intermediates.[170] However, the poor structural stability is a common problem for the 2D MOFs directly working as the electrocatalysts. For example, if the organic ligands in MOFs are labile in the electrochemical reactions, the coordinatively unsaturated metal centers would be generated and result in poor long-term stability. Usually, thinner 2D MOFs exhibit more serious crystal structure damages during the electrocatalysis. Some techniques such as *in situ* XRD and FT-IR analysis could be employed to recognize the structural evolution of the MOFs within the electrocatalysis in order to better understand the catalytic mechanism and design more stable MOF-based electrocatalysts. The structural stability issue needs to be tackled before the 2D MOFs could be practically used in electrocatalysis.

4. 2D MOF derivatives for electrochemical energy storage and electrocatalysis

Although a number of 2D MOFs have been employed as electrochemical energy storage materials and electrocatalysts in the past few years, the unsatisfactory conductivity and stability still hinder their further applications in these fields. Nevertheless, the 2D MOF derivatives (which can be easily obtained from the

2D MOF precursors through a simple thermal treatment in different atmospheres), such as carbon materials, metal, metal compounds, and their composites, with improved physical and chemical properties as well as new functions have attracted increasing attention for electrochemical energy storage and electrocatalysis. In this section, we highlight some promising applications of 2D MOF derivatives in batteries, SCs, OER, HER, ORR, and CO_2RR.

4.1. 2D MOF derivatives for electrochemical energy storage

2D MOF derivatives with an ultrahigh specific area and well-defined pore distribution demonstrate a large number of active sites for ion storage, exhibiting a great potential for energy storage devices (Table 3). In this section, we highlight some of the 2D MOF derivatives, such as carbon nanosheets, inorganic metal compound nanosheets, and their composites, as the electrode materials in batteries and SCs.

4.1.1. 2D MOF derivatives for batteries. 2D carbon nanosheets derived from 2D MOFs were reported by our group and applied in LIBs.[101] As shown in Fig. 19a and b, through a simple carbonization, ultrathin 2D Zn(bim)(OAc) nanosheets with an average thickness of about 5.2 nm were transformed into ultrathin carbon nanosheets (UT-CNSs) with a thickness of 2.5 $\pm$ 0.8 nm. Fig. 19c shows the rate performance of the UT-CNSs as the LIB anode materials, where the UT-CNSs could reach an initial capacity of 2493 mA h g^{-1} and maintained a reversible capacity of 1229 mA h g^{-1} at the current density of 100 mA g^{-1} (Fig. 19d and e). Moreover, even at a high current density of 10 A g^{-1}, the UT-CNSs still exhibited a high capacity of 553 mA h g^{-1}, implying excellent rate performance (Fig. 19f and g). The high capacity and excellent rate performance were mainly due to the superior conductivity and ultrathin morphology of the UT-CNSs. Moreover, compared to other templated CNSs, the UT-CNSs derived from 2D MOFs had controllable pore distribution with more mesopores, which are the superior qualities for energy storage.[180]

In addition, porous inorganic metal compounds and their carbon-based composites derived from 2D MOFs have also attracted intensive attention as the anode materials for LIBs in recent years. For instance, 2D mesoporous hetero-$ZnFe_2O_4$/ZnO nanosheets (ZFOZ NSs) derived from $Zn_3[Fe(CN)_6]$ were employed as the anode for LIBs and exhibited long-life cycling behaviors and large reversible capacities at high rates.[173] Other 2D MOF-derived metal oxides and their inorganic composites, such as Co_3O_4,[181] Co_3O_4–NiO,[182] Fe_3O_4@NC,[25] and CoO@C,[29] also exhibited excellent lithium-ion storage ability. Especially, CoO@C, with the advantages of both metal oxides and carbon materials, showed excellent LIB performance. As shown in Fig. 19h–i, the CoO nanoarrays with a thin carbon layer on the surface (CoO@C) were directly derived from 2D Kagóme MOF nanoarrays. Benefiting from the well-organized core–shell structure, CoO@C exhibited a highly reversible capacity of 1003 mA h g^{-1} for over 200 cycles at the current density of 0.2 A g^{-1}, superior rate capability (620 mA h g^{-1} at 2 A g^{-1}), and excellent cycling stability (Fig. 19j–l).

2D MOF derivatives also show great potential for other batteries, such as SIBs, Li–S batteries, and Zn–air batteries.[48,183–185] It is well known that the diffusion of Na^+ in the electrodes is more difficult than that of Li^+ due to the larger radius of Na^+.[186] Thus, the electrode materials for SIBs require more mesopores and larger interlayer distances for the Na^+ intercalation.[109,111,187] 2D MOF derivatives with an ultrathin morphology and hierarchical pore structure were widely employed as the suitable electrode candidates for SIBs.[188] For example, Fang and co-workers fabricated a leaf-like 2D CoZn-MOF, which was then directly converted to a Co_3O_4/ZnO hybrid.[174] Due to the homogeneous distributions of Co_3O_4 and ZnO, the Co_3O_4/ZnO hybrid exhibited a high rate property of 242 mA h g^{-1} at 2 A g^{-1}. Moreover, the harmonious multi-step conversion reaction of Co_3O_4 and ZnO was helpful for volume buffering, leading to outstanding cycling stability (with capacity retention of 91% after 1000 cycles at 2 A g^{-1}). In addition, this kind of leaf-like 2D Co-MOFs could also be converted to other inorganic metal compounds, which could further boost the performance of SIBs.[174] The Wu group developed a versatile and scalable protocol for the synthesis of 2D holey cobalt sulfide (h-Co_4S_3) from leaf-like 2D Co-MOFs (Fig. 20a–c).[176] Benefiting from the 2D nanosheet nature with in-plane mesopores (with

Table 3 The performance of different 2D MOF derivatives used for LIBs, SIBs, and SCs

Materials	Application	Thickness/nm	Specific capacity	Rate performance	Cycles	Ref.
NCH	LIB	3.7	609 mA h g^{-1} at 1 A g^{-1}	510 mA h g^{-1} at 2 A g^{-1}	500	171
UHCS-900	LIB	1–2	750 mA h g^{-1} at 0.5C	700 mA h g^{-1} at 1C	250	172
NCW@Fe_3O_4/NC	LIB	N/A	1741 mA h g^{-1} at 1 A g^{-1}	723 mA h g^{-1} at 10 A g^{-1}	600	25
$ZnFe_2O_4$/ZnO NSs	LIB	2–10	537 mA h g^{-1} at 0.5 A g^{-1}	266 mA h g^{-1} at 1.5 A g^{-1}	500	173
Co_3O_4/ZnO	LIB	109	716 mA h g^{-1} at 1 A g^{-1}	404 mA h g^{-1} at 4 A g^{-1}	1000	174
CoO@C	LIB	N/A	991 mA h g^{-1} at 0.2 A g^{-1}	587 mA h g^{-1} at 2 A g^{-1}	300	29
NPCNs	SIB	2.7–6	322 mA h g^{-1} at 0.1 A g^{-1}	194 mA h g^{-1} at 10 A g^{-1}	1000	175
h-Co_3O_4 NSs	SIB	10–30	571 mA h g^{-1} at 0.1 A g^{-1}	257 mA h g^{-1} at 12 A g^{-1}	400	176
$NiSe_2$/NC	SIB	6	410 mA h g^{-1} at 1 A g^{-1}	255 mA h g^{-1} at 10 A g^{-1}	1000	58
$NiFe_2$@NCNs	SIB	10	289 mA h g^{-1} at 0.1 A g^{-1}	268 mA h g^{-1} at 10 A g^{-1}	5000	177
$Ni(OH)_2$@ZnCoS NSs	SC	120	2730 F g^{-1} at 3 mA cm^{-2}	390 mF cm^{-2} at 15 mA cm^{-2}	10 000	33
CoSNC	SC	42	360 F g^{-1} at 1.5 A g^{-1}	205 F g^{-1} at 30 A g^{-1}	2000	178
APC	SC	3.5	260 F g^{-1} at 0.5 A g^{-1}	165 F g^{-1} at 10 A g^{-1}	5000	47
CC@Co_3O_4	SC	100–150	322 F g^{-1} at 6.25 A g^{-1}	260 F g^{-1} at 100 A g^{-1}	10 000	179

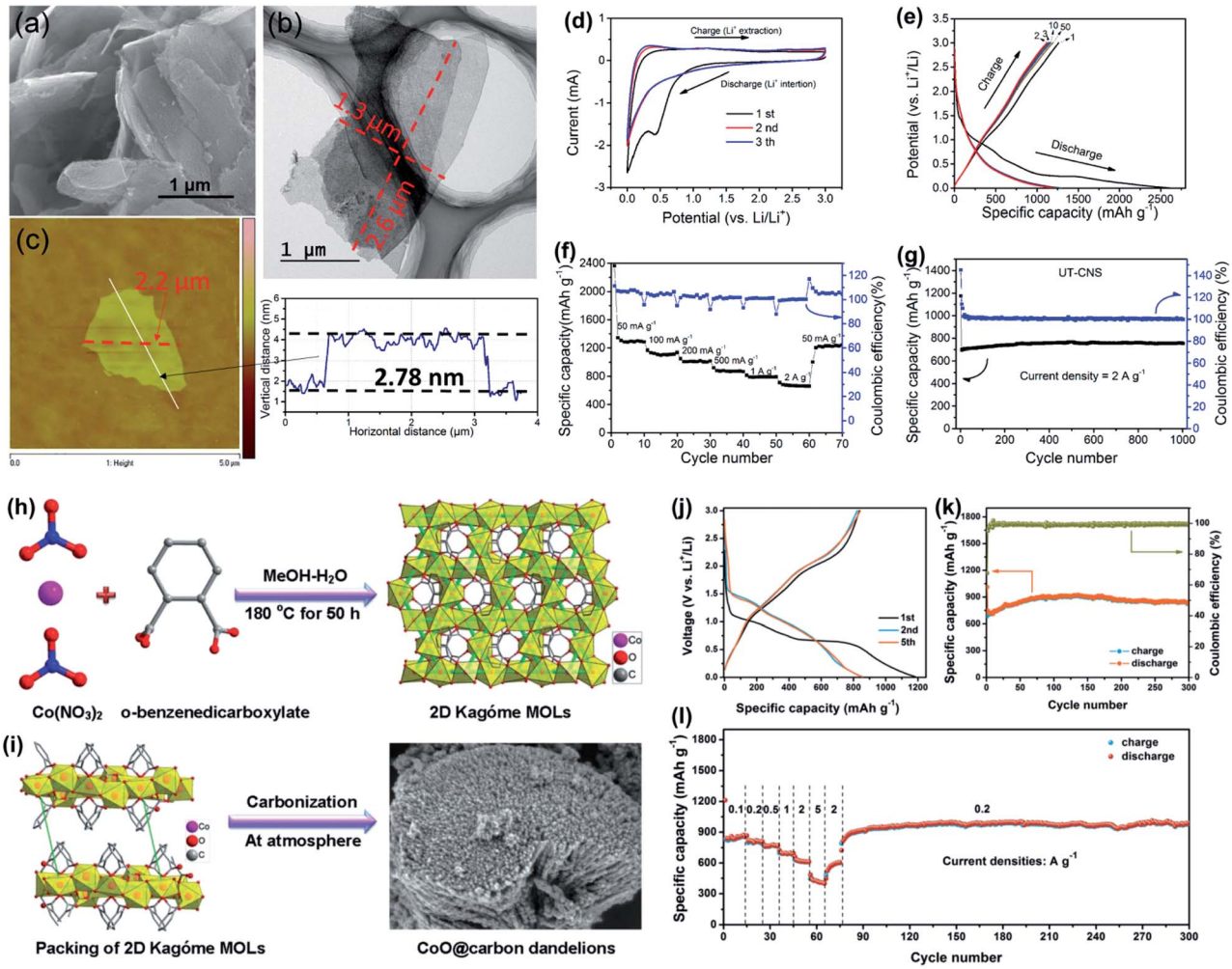

Fig. 19 Morphologies of UT-CNS and performance of UT-CNS as the anode material for LIBs. (a) SEM, (b) TEM, (c) AFM images with measured dimensions, (d) CV curves at the scan rate of 0.5 mV s^{-1}, (e) charge–discharge profiles at the current density of 100 mA g^{-1}, (f) rate performance at current densities from 100 to 10 000 mA g^{-1}, and (g) cycling performance at the current density of 2 A g^{-1} for 1000 cycles. Reproduced with permission.[101] Copyright©2018 The Royal Society of Chemistry. (h) Schematic illustration of the synthesis process of CoO@carbon dandelions. (i) Stacking of two 2D MOLs in one-unit cell as revealed by X-ray single crystal analysis and FESEM image of the as-synthesized CoO@carbon dandelions. (j) Charge–discharge curves, (k) cycling performance and (l) rate performance of CoO@carbon dandelions. Reproduced with permission.[29] Copyright©2018 WILEY-VCH Verlag GmbH & Co. KGaA.

a diameter of 2–30 nm), ultrathin morphology (<30 nm), and microscale lateral size providing more active sites and enhanced sodiation/desodiation kinetics, h-Co_4S_3 exhibited a high reversible capacity of 571 mA h g^{-1} at 0.1 A g^{-1} (Fig. 20d). Moreover, the h-Co_3S_4 had the highest rate capacity of 254 mA h g^{-1} at a charge–discharge current density of 12 A g^{-1} among the reported cobalt sulfide-based SIB anodes (Fig. 20e).

Carbon materials and inorganic metal compound/carbon composites with better conductivity are regarded as more suitable candidates for SIBs. Liu and co-workers reported a simple method to prepare ultrathin nitrogen-doped porous carbon nanosheets (NPCNs) from 2D layered MOFs (Zn-hexamine, Zn-HMT) (Fig. 20f).[175] The SEM characterizations reveal the successful fabrication of NPCNs (Fig. 20h) from Zn-HMT nanosheets (Fig. 20g) and the AFM result shows that the thickness of the as-prepared NPCNs is about 4.5 nm (Fig. 20i). Due to the high N content in the HMT, an ultrahigh N-doping level (16.64 at%) was realized in the NPCNs. The N-doping in the ultrathin carbon nanosheets could significantly enhance the interlayer distance of the carbon lattice and provide abundant active sites, which therefore significantly improves the sodium storage performance of the carbon-based materials. In addition, the mesopores originating from the removal of the Zn-based contents could enhance the ion-diffusion property of the NPCNs as the anode materials for SIBs. As a proof-of-concept application, the NPCNs exhibited a high reversible capacity of 318 mA h g^{-1} at 0.1 A g^{-1} and maintained a high rate performance with a capacity of 194 mA h g^{-1} even at a high current density of 10 A g^{-1} for SIBs (Fig. 20j and k). In addition, the HMT, as a universal organic linker, could easily coordinate with the transition metal ions by using different coordination modes, which were used to synthesize the metal-HMT and its

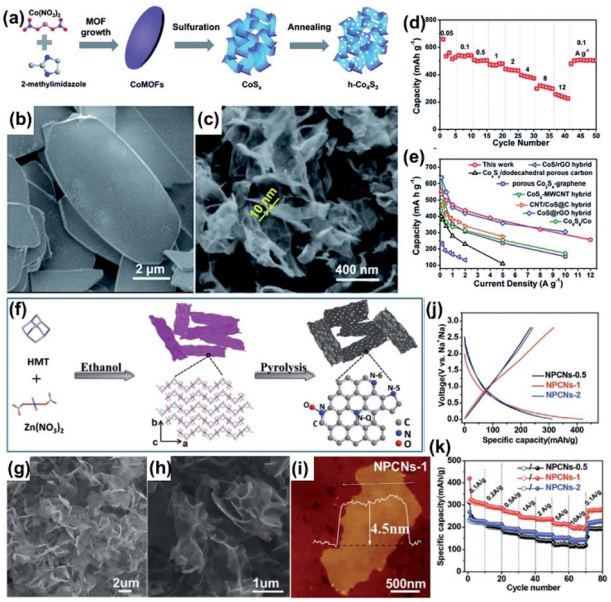

Fig. 20 2D MOF derivatives for SIBs. (a) Schematic illustration of the fabrication of h-Co_4S_3 and SEM images of (b) CoMOFs and (c) h-Co_4S_3. (d) Rate performance of h-Co_4S_3 as SIB anodes. (e) Rate performance comparison studies of h-Co_4S_3 with other CoS_x composites. Reproduced with permission.[176] Copyright©2018 The Royal Society of Chemistry. (f) Schematic illustration of the preparation of Zn-HMTs and their derivatives (NPCNs). (g) SEM images of Zn-HMT nanosheets. (h) SEM and (i) AFM images of NPCNs. (j) Charge–discharge and (k) rate performance curves of NPCNs as the SIB anodes. Reproduced with permission.[175] Copyright©2018 WILEY-VCH Verlag GmbH & Co. KGaA.

derived inorganic metal compounds/C composites toward superior SIB anodes. Later on, the same group reported a series of Ni-based inorganic metal compounds/C (*e.g.*, $NiSe_2$/NC,[58] $NiTe_2$/NC,[177] and Ni/NC[189]) by using Ni-HMT nanosheets as the precursors, which displayed much better performance for SIBs than the NPCNs.

Besides, 2D MOF derivatives can also be used as the electrode materials in Li–S batteries due to their variable surface elemental compositions and suitable pore distribution for S storage. For instance, the Zhang group reported a thermal method to *in situ* thermo-exfoliate layered 2D MOFs into ultrahydrophilic graphene stacks (UHCS) with a highly polar carbon surface, hierarchically porous structure, and defined uniform nanosheet morphology.[172] This kind of porous carbon could well cage-confine the polysulfides and provide a fine electron and ion accessible environment. Therefore, a reversible manner of the coupled redox reaction was achieved in UHCS as the electrode of Li–S batteries.

4.1.2. 2D MOF derivatives for SCs. As discussed in Section 3.1.2, 2D MOFs with a high accessible area and short ion-diffusion distance are regarded as suitable electrode materials for SCs. However, the unsatisfactory conductivity of the conventional MOFs and the as-prepared conjugated 2D MOFs still hinder their wide application in SCs. Thus, in most cases, 2D MOFs are converted to carbon nanosheets or inorganic metal compounds/C composites for better application in SCs.

The aforementioned UT-CNSs derived from UT-Zn(bim)(OAc) developed by our group could not only be used in LIBs, but also exhibited excellent performance while employed as electrode materials in SCs.[101] Benefiting from their high electrical conductivity (due to the high degree of graphitization), low contact resistance of the 2D materials, and large ultrathin nanosheet morphology with a high-porosity structure, the UT-CNSs showed a high capacitance of 347 F g^{-1} at the current density of 0.5 A g^{-1}. Even at a high current density of 10 A g^{-1}, the UT-CNSs still presented a high gravimetric capacitance of 283 F g^{-1}. In addition to the 2D MOF-derived carbon nanosheets, the inorganic metal compounds/C materials derived from the 2D MOFs with pseudocapacitive behaviors were extensively investigated as the possible electrode materials for SCs. For instance, Cao and co-workers reported 2D MOF-derived 2D $CoS_{1.097}$/nitrogen-doped carbon nanocomposites (CoSNCs).[178] As shown in Fig. 21a, 2D porphyrin paddlewheel framework-3 (PPF-3) MOF nanosheets (Fig. 21b) with a thickness of *ca.* 12–43 nm (Fig. 21c) were synthesized by using $Co_2(COO)_4$ and TCPP as the reactants and 4,4′-bipyridine (BPY) as the intercalation agent. Then, the PPF-3 nanosheets were directly carbonized to the CoSNCs. As shown in Fig. 21d, the nanosheet morphology was retained after the carbonization. The top inset in Fig. 21d shows that the $CoS_{1.097}$ nanodots are uniformly distributed in the carbon matrix. All CV curves (Fig. 21e) of the 2D CoSNC nanocomposite electrode exhibit rectangular shapes with distinct redox peaks, which indicates that the capacitance characteristics of this nanocomposite are governed by both the faradaic redox reactions and EDLC behaviors. The 2D CoSNCs also delivered a much higher specific capacitance than that of the bulk CoSNC electrode (Fig. 21f). Besides, the 2D carbon nanosheets and 2D inorganic metal compounds/C derived from the 2D MOFs could also be employed as the positive and negative electrodes for the asymmetric SCs, respectively. As shown in Fig. 21g, the Co-MIM nanosheets were firstly grown on carbon cloth, which were then directly converted to the carbon nanosheets (CC@NCN) and Co_3O_4 nanosheets (CC@Co_3O_4) in different atmospheres.[179] CC@NCN (Fig. 21h) and CC@Co_3O_4 (Fig. 21i) exhibited highly porous nanosheet morphologies. The asymmetric SCs assembled with CC@NCN and CC@Co_3O_4 exhibited a maximum energy density of 41.5 W h kg^{-1} with a power density of 6.2 kW kg^{-1} (Fig. 21j), and delivered excellent durability with the capacitance retention of 90.8% and 85.5% (compared to the initial capacitance) after 10 000 and 20 000 cycles, respectively (Fig. 21k). CC@NCN could also be employed as a superior substrate to load different inorganic metal compounds (*e.g.*, MnO_2 (ref. 27) and ZnCoS[33]) to enhance the pseudocapacitive performance.

4.2. 2D MOF derivatives used as electrocatalysts

Facile approaches to synthesize 2D MOFs provide an effective way to obtain MOF derivatives with structural complexity and tunable compositions.[190–192] Owing to the ordered arrangement of the metal ions and organic ligands in the MOF crystals, the obtained MOF derivatives usually have nanoporous structures

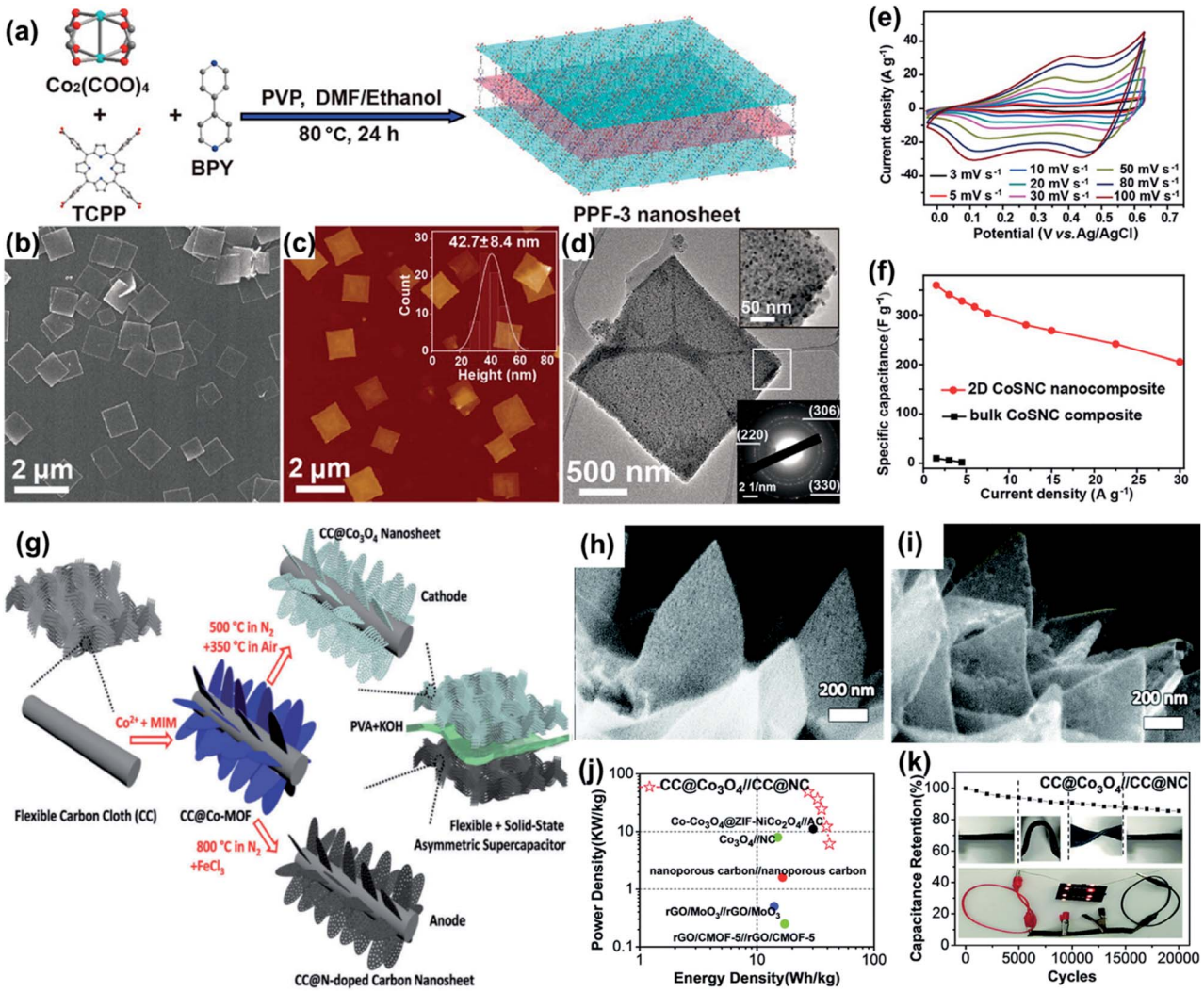

Fig. 21 (a) Schematic illustration of the synthesis process of PPF-3 nanosheets. (b) SEM image and (c) AFM image of PPF-3 nanosheets. Inset: Statistical analysis of the thickness of 75 PPF-3 nanosheets measured in AFM images. (d) TEM images of CoSNC. (e) CV and (f) galvanostatic charge/discharge curves of the 2D CoSNC nanocomposite electrode measured in 2.0 M KOH. Reproduced with permission.[178] Copyright©2016 American Chemical Society. (g) Schematic illustration of a flexible asymmetric supercapacitor. SEM image of (h) CC@NCN and (i) CC@Co_3O_4. (j) Ragone plots and (k) cycling test result of the asymmetric supercapacitor with PVA–KOH gel electrolyte. Reproduced with permission.[179] Copyright©2017 The Royal Society of Chemistry.

and uniform distribution of different components (*e.g.*, metal nanoparticles and carbon).[25,193] Moreover, the organic ligands in MOFs enable the formation of carbon-based nanomaterials after carbonization, leading to the improvement of the electrical conductivity and electrochemical activity for the MOF derivatives.[194] In this section, we highlight some promising applications of 2D MOF-derived materials for the electrocatalysis of the OER, HER, and ORR.

4.2.1. 2D MOF derivatives for the OER and HER. 2D MOFs are promising precursors or templates for electrocatalysts owing to their ability of tuning the inherent electronic and/or surface structure of the derivatives and endowing the resultant products with hollow or porous nanostructures.[36,195] The derivatives of 2D MOF nanosheets, such as 2D metal oxides, metal phosphates, and porous carbon based materials, have been investigated as the electrocatalysts for the OER and HER.

The derivatives of the Fe-, Co-, and Ni-based 2D MOF nanosheets are considered as high-performance electrocatalysts for the OER due to the high concentration of Fe, Co, and Ni atoms/ions distributed on the surface of the electrocatalysts, which can form catalytically active sites during the OER process, such as the Co(IV)–OH and Ni(IV)–OH intermediates. Fan *et al.* template-grew Ni-doped ZIF-67 nanosheets on Mxenes ($Ti_3C_2T_x$) and then directly converted them to NiCoS/$Ti_3C_2T_x$ composites through a heat treatment in the presence of sufficient S powder. NiCoS/$Ti_3C_2T_x$ exhibited a low OER overpotential of 365 mV at 10 mA cm^{-2} and Tafel slope of 58.2 mV dec^{-1}.[196] Wang fabricated a series of $Co_{1-x}Fe_xP$ nanoparticles embedded in 2D MOF-derived carbon nanosheets and investigated their electrocatalytic activities toward the OER.[197] As shown in Fig. 22a and b, $Co_{0.7}Fe_{0.3}$-MOF nanosheets and $Co_{0.7}Fe_{0.3}P$/C nanosheets are successfully obtained. The HRTEM image of $Co_{0.7}Fe_{0.3}P$/C

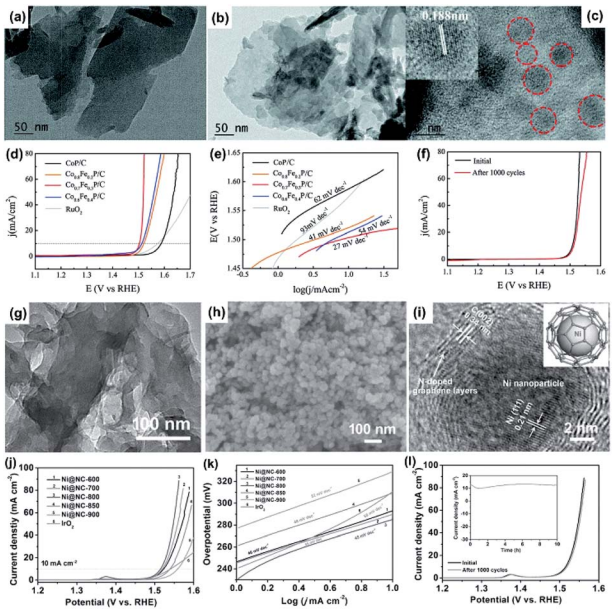

Fig. 22 TEM images of (a) $Co_{0.7}Fe_{0.3}$-MOF nanosheets and (b) $Co_{0.7}Fe_{0.3}P$/C nanosheets. (c) HRTEM image of $Co_{0.7}Fe_{0.3}P$/C nanosheets. (d) LSV curves and (e) the corresponding Tafel plots of $Co_{1-x}Fe_xP$/C nanosheets and commercial RuO_2 catalyst in 1 M KOH solution. (f) Polarization curves of the $Co_{0.7}Fe_{0.3}P$/C catalyst before and after 1000 potential cycles. Reproduced with permission.[197] Copyright ©2018 The Royal Society of Chemistry. (g) TEM image of Ni-BDC nanosheets. (h) SEM and (i) HRTEM images of Ni@NC. (j) The OER polarization curves and (k) the corresponding Tafel plots of various Ni@NC samples and commercial IrO_2 catalyst in 1.0 M KOH solution. (l) Polarization curves of the Ni@NC-800 catalyst before and after 1000 potential cycles. The inset of (l) is the chronoamperometric curve at 1.52 V (*vs.* RHE).[198] Copyright©2017 WILEY-VCH Verlag GmbH & Co. KGaA.

indicates that the $Co_{1-x}Fe_xP$ nanoparticles are embedded in the carbon nanosheets (Fig. 22c). The experimental results demonstrated that moderate iron doping could preserve the catalytically active sites. Hence, the $Co_{0.7}Fe_{0.3}P$/C had the best activity with an overpotential of about 270 mV to reach an OER current density of 10 mA cm^{-2} (Fig. 22d) and a low Tafel slope of 27 mV dec^{-1} (Fig. 22e). Furthermore, $Co_{0.7}Fe_{0.3}P$/C also barely delivered overpotential increase after 1000 cycles as the electrocatalyst for the OER in 1 M KOH (Fig. 22f). Attributed to the excellent spatial confinement of 2D materials, the sizes of metals or metal inorganic compounds derived from the 2D MOF nanosheets could be flexibly regulated by the thickness of the 2D MOF precursors. For instance, sub-10 nm uniformly distributed nickel nanoparticles encapsulated in few-layer nitrogen-doped graphene (Ni@NC) could be facilely prepared by using ultrathin Ni-BDC nanosheets as the precursor through a high-temperature annealing treatment (Fig. 22g and h).[198] Owing to its ultrasmall particle size and complete carbon coating (Fig. 22i), Ni@NC displayed an anodic current density of 10 mA cm^{-2} at an overpotential of 280 mV (Fig. 22j) with a Tafel slope as low as 45 mV dec^{-1} (Fig. 22k) as well as excellent stability (Fig. 22l).

2D MOF derivatives with a high accessible surface area and inhomogeneous plane electron distribution were also used as catalysts for the HER. For instance, Lee reported a 2D MOF-derived Co/N-doped carbon electrocatalyst for the HER.[199] Owing to its low H-atom binding energy on metallic cobalt and high conductivity and stability of the carbon-encapsulated Co nanoparticles, Co/N–carbon exhibited an outstanding activity with a small overpotential of 103 mV at 10 mA cm^{-2}. Luo synthesized CoP nanoparticles encapsulated in an ultrathin nitrogen-doped porous carbon shell (CoP@NC) using ZIF-9 as the precursor *via* a two-step MOF-derivation route.[200] Compared to CoP@C (η_{10} = 130 mV) and CoP (η_{10} = 128 mV), CoP@NC presented excellent performance with an overpotential of 78 mV at 10 mA cm^{-2} and Tafel slope of 49 mV dec^{-1}. The DFT calculation demonstrated that the dopants, CoP and N, were beneficial to optimizing the binding energy of the H species on the active sites and therefore led to better HER activity. Moreover, a number of 2D MOF derivatives can also work as bifunctional catalysts for both the OER and HER. Du fabricated phosphide–carbon nanosheet composites from 2D cobalt porphyrinic MOF nanosheets, which consisted of cobalt phosphide nanoparticles embedded in mesoporous N-doped graphitic carbon materials.[36] This catalyst exhibited good electrocatalytic activities for the HER in 0.5 M H_2SO_4 and the OER in 1 M KOH with overpotentials of 98 and 370 mV at 10 mA cm^{-2} and the Tafel slopes of 74 and 79 mV dec^{-1}, respectively.

4.2.2. 2D MOF derivatives for the ORR. 2D MOF derivatives with excellent dimensional properties (*e.g.* a high surface area, suitable pore distribution, and abundant active sites) have been considered as high-performance catalysts for the ORR.[201] For example, 2D-hexagonal-leaf-like ZIF lamellae (ZIF-L) derived ceria@2D-hexagonal-leaf-like hierarchical porous carbon nanosheets (CeO_2–HPCN) reached a positive onset potential of 0.923 V for the ORR, which is quite similar to that of commercial Pt/C.[202] In addition, ZIF-67 can also be converted to 2D carbon-based materials for the ORR due to its transformation into a special 2D form during the heat treatment.[60,183,203–205] For instance, graphene-like N,Co-CNSs derived from the ZIF-67 polyhedra *via* the molten salt method exhibited comparable catalytic performance toward the ORR as the ZIF-L derived materials. Furthermore, Huang and coworkers reported a facile method to fabricate a 2D Co–N codoped carbon based electrocatalyst (Co,N-CNS) by directly carbonizing the NaCl-caged 2D Co-MIM MOFs.[60] The optimized Co,N-CNS-800 °C exhibited an ORR $E_{1/2}$ of 0.869 V_{RHE}, which was 23 mV more positive than that of Pt/C. 2D MOFs synthesized by using LDHs as the templates were also used to synthesize 2D MOF derivatives as the catalysts for the ORR. Li and coworkers directly grew ZIF-67 on a Co-containing LDH, which could be directly converted to a honeycomb-like Co-doped carbon material (LDH@ZIF-67-800).[207] Owing to its hierarchical structure, the LDH@ZIF-67-800 delivered excellent catalytic performance with an $E_{1/2}$ of 0.83 V_{RHE} as well as a large diffusion-limiting current density of 5.5 mA cm^{-2}. In addition, layered $FeCl_3 \cdot 6H_2O$ crystals could also be employed to prepare organic–metal complexes by using dopamine hydrochloride (DA·HCl) as the linker. As shown in Fig. 23a, the DA molecules were assembled in the interlayer of

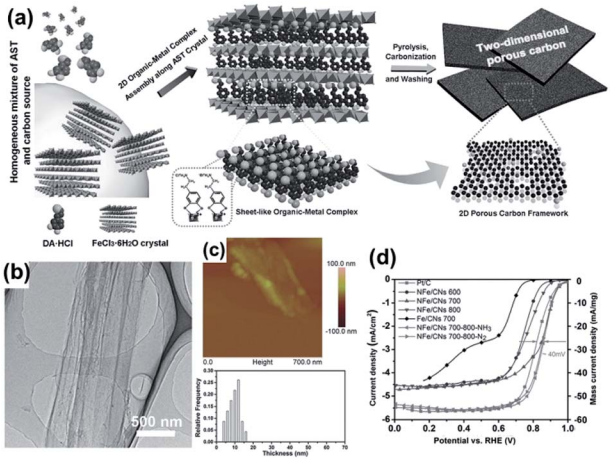

Fig. 23 (a) Schematic illustration of the overall synthetic procedure of 2D microporous carbon nanosheets (CNs). Representative (b) TEM, (c) AFM images, and corresponding thickness distribution based on 50 height section measurements of NFe/CNs-700. (d) RDE polarization curves of Pt/C, Fe/CNs-700, and NFe/CN catalysts prepared at different temperatures. The catalyst loading amount is 0.1 mg cm^{-2} for all samples. Reproduced with permission.[206] Copyright ©2017 WILEY-VCH Verlag GmbH & Co. KGaA.

the $FeCl_3 \cdot 6H_2O$ crystals, which were then directly converted to the N,Fe-codoped 2D porous carbon nanosheets (NFe/CNs).[206] The TEM image shows that 2D NFe/CNs 700 has a wrinkle sheet morphology (Fig. 23b). The AFM image and statistical thickness distribution based on 50 height section measurements reveal that the thickness of NFe/CNs 700 is about 10 nm (Fig. 23c). Finally, the ORR performances of the as-prepared NFe/CNs and commercial Pt/C were studied in 0.1 M KOH electrolyte. Among them NFe/CNs 700 achieved a high $E_{1/2}$ of 0.863 V_{RHE} with a limiting current density of 5.45 mA cm^{-2}, which was about 40 mV higher than that on Pt/C (Fig. 23d).

4.2.3. 2D MOF derivatives for other catalysis. Single atom catalysts (SACs) have attracted intensive attention due to their excellent catalytic performance. Accordingly, SACs have the advantage of nearly 100% atom utilization. The bulk MOFs, especially ZIF-8 and ZIF-67, were considered as suitable precursors for the production of SACs due to that the stable coordinated structures of metal ions and linkers could efficiently prevent the aggregation of the metal ions during the carbonization process. However, the low yield and low metal site utilization of the bulk-like morphology have limited the practical application of the bulk MOFs as the precursors for SACs. In contrast, 2D MOF nanosheets, with a high surface area and low thickness, were regarded as more suitable precursors for SACs. For instance, Zuo and coworkers achieved an ultrahigh single Pt atom loading of 12.2 wt% by carbonizing Pt-TCPP nanosheets.[208] Besides, although some of the 2D MOF derived SACs have a low metal loading, they still render ultrahigh catalytic activity. For example, the Li group reported an ultrathin 2D nitrogen-doped carbon (Co SAs/2D N–C) with a low Co-loading of 0.15 wt%. Owing to the high accessible surface area and high metal utilization, Co SAs/2D N–C achieved exceptional catalytic activity and selectivity for the selective oxidation of silanes.[209]

5. Conclusions

In this review, some recent significant research progress on the synthesis and applications of 2D MOFs and their derivatives is summarized. First, we thoroughly reviewed the synthetic strategies that have been developed for the 2D MOFs, including the representative methods in both top-down and bottom-up approaches. The mechanisms and the applicability of these synthetic strategies are discussed. Then, the typical applications of 2D MOFs and their derivatives for electrochemical energy storage and electrocatalysis are reviewed. The advantages and drawbacks of the 2D MOFs and their derivatives in these applications are discussed.

Generally, the synthesis of high-quality 2D MOFs with a high yield and at a low cost is one of the most critical challenges in the development and application of 2D MOFs and their derivatives. Although much effort has been made, some significant challenges toward the practical application of the 2D MOFs and their derivatives for energy storage and electrocatalysis still exist.

(1) High-quality and scalable fabrication of the 2D MOFs still needs continuous efforts. Both modifications/upgrades of the currently existing synthetic strategies and the development of novel synthetic methods to achieve better quality, higher yield, and lower cost of the 2D MOFs are welcome. Regarding the novel synthetic methods, electrochemical deposition, as a kind of facile and economical synthesis method, might be a possible solution since it could directly fabricate target materials on conducting or semiconducting substrates (*i.e.*, the current collectors of the electrodes in energy storage and electrocatalysis) with better conductivity compared to the powdery material-based electrodes. To the best of our knowledge, facile electrodeposition of 2D MOFs with a controllable morphology and composition has not been achieved.

(2) The poor stability of the 2D MOFs hinders their wide applications. Thus, constructing highly stable 2D MOFs with strong coordination bonds is highly demanded in the future for their applications under critical conditions such as for the OER. The MOF structures with strong coordination bonds or significant steric hindrance could possibly prevent the metal–ligand coordination bonds from hydrolysis. Such strong metal–ligand bonds could be probably designed based on the hard/soft acid/base rule (*i.e.* the hard-acid metal ions coordinate with hard-base ligands such as CH_3COO^-, and the soft-acid metal ions coordinate with the soft-base ligands such as CN^-).

(3) The currently reported conductive MOFs are all based on high-cost organic ligands, which are far from practical application. Thus, exploration of low-cost ligands for the construction of conductive MOF nanosheets is urgently needed. For example, square-planar $Cu(NH)_4$ and $Ni(NH)_4$ nodes with a d–π conjugation could probably be used to design and fabricate highly conductive MOF nanosheets.

(4) The high tendency to agglomerate is another issue for 2D MOFs. Although some strategies have been developed to prevent 2D MOFs from agglomeration, more efficient and economical methods are still desired.

(5) The destruction of the pore structure and ordered surface metal node arrangement during the transformation from the 2D MOFs to their derivatives is still one of the biggest issues for the application of the 2D MOF derivatives. Thus, the development of strategies to convert 2D MOFs to their 2D derivatives while better maintaining the structural properties is highly demanded in future research.

Conflicts of interest

There are no conflicts to declare.

Acknowledgements

This work was supported by the National Natural Science Foundation of China (grant no. 51772332), the Hunan Provincial Science and Technology Plan Project (grant no. 2018RS3008 and 2017TP1001), and the Natural Science Foundation of Hunan Province (grant no. 2018JJ2485).

Notes and references

1 X. Yang, C. Cheng, Y. Wang, L. Qiu and D. Li, *Science*, 2013, **341**, 534–537.
2 T.-S. Kim, H. J. Song, M. A. Dar, H.-W. Shim and D.-W. Kim, *J. Am. Ceram. Soc.*, 2018, **101**, 3749–3754.
3 Y. Wang, Y. Song and Y. Xia, *Chem. Soc. Rev.*, 2016, **45**, 5925–5950.
4 X. Yang, A.-Y. Lu, Y. Zhu, M. N. Hedhili, S. Min, K.-W. Huang, Y. Han and L.-J. Li, *Nano Energy*, 2015, **15**, 634–641.
5 Q. Wang, J. Yan and Z. Fan, *Energy Environ. Sci.*, 2016, **9**, 729–762.
6 L. Wang and X. Hu, *Chem.–Asian J.*, 2018, **13**, 1518–1529.
7 X. Cao, C. Tan, M. Sindoro and H. Zhang, *Chem. Soc. Rev.*, 2017, **46**, 2660–2677.
8 C. H. Hendon, A. J. Rieth, M. D. Korzynski and M. Dinca, *ACS Cent. Sci.*, 2017, **3**, 554–563.
9 H. Wang, Q.-L. Zhu, R. Zou and Q. Xu, *Chem*, 2017, **2**, 52–80.
10 S. Dutta, Z. Liu, H. Han, A. Indra and T. Song, *ChemElectroChem*, 2018, **5**, 3571–3588.
11 Z. Jiang, T. Liu, L. Yan, J. Liu, F. Dong, M. Ling, C. Liang and Z. Lin, *Energy Storage Materials*, 2018, **11**, 267–273.
12 G. Ye, Q. He, S. Liu, K. Zhao, Y. Su, W. Zhu, R. Huang and Z. He, *J. Mater. Chem. A*, 2019, **7**, 16508–16515.
13 X.-L. Wang, L.-Z. Dong, M. Qiao, Y.-J. Tang, J. Liu, Y. Li, S.-L. Li, J.-X. Su and Y.-Q. Lan, *Angew. Chem., Int. Ed.*, 2018, **57**, 9660–9664.
14 Y. Wang and C. Woell, *Catal. Lett.*, 2018, **148**, 2201–2222.
15 Q. Yang, Q. Xu and H.-L. Jiang, *Chem. Soc. Rev.*, 2017, **46**, 4774–4808.
16 M. G. Campbell, S. F. Liu, T. M. Swager and M. Dinca, *J. Am. Chem. Soc.*, 2015, **137**, 13780–13783.
17 S. Homayoonnia and S. Zeinali, *Sens. Actuators, B*, 2016, **237**, 776–786.
18 D. Ning, Q. Liu, Q. Wang, X.-M. Du, W.-J. Ruan and Y. Li, *Sens. Actuators, B*, 2019, **282**, 443–448.
19 R. Xu, Y. Wang, X. Duan, K. Lu, D. Micheroni, A. Hu and W. Lin, *J. Am. Chem. Soc.*, 2016, **138**, 2158–2161.
20 X. Zhao, Y. Wang, D.-S. Li, X. Bu and P. Feng, *Adv. Mater.*, 2018, **30**, 1705189.
21 Y. Hua, H. Wang, Q. Li, G. Chen, G. Liu, J. Duan and W. Jin, *J. Mater. Chem. A*, 2018, **6**, 599–606.
22 Y. Peng, Y. Li, Y. Ban, H. Jin, W. Jiao, X. Liu and W. Yang, *Science*, 2014, **346**, 1356–1359.
23 H. Li, K. Wang, Y. Sun, C. T. Lollar, J. Li and H.-C. Zhou, *Mater. Today*, 2018, **21**, 108–121.
24 M. A. N. Khan, P. K. Klu, C. Wang, W. Zhang, R. Luo, M. Zhang, J. Qi, X. Sun, L. Wang and J. Li, *Chem. Eng. J.*, 2019, **363**, 234–246.
25 Y. Wang, Y. Gao, J. Shao, R. Holze, Z. Chen, Y. Yun, Q. Qu and H. Zheng, *J. Mater. Chem. A*, 2018, **6**, 3659–3666.
26 J. Cong, H. Xu, M. Lu, Y. Wu, Y. Li, P. He, J. Gao, J. Yao and S. Xu, *Chem.–Asian J.*, 2018, **13**, 1485–1491.
27 X. Liu, C. Guan, Y. Hu, L. Zhang, A. M. Elshahawy and J. Wang, *Small*, 2018, **14**, 1702641.
28 W. Shuang, L. Kong, M. Zhong, D. Wang, J. Liu and X.-H. Bu, *Dalton Trans.*, 2018, **47**, 12385–12392.
29 F. Wu, S. Zhang, B. Xi, Z. Feng, D. Sun, X. Ma, J. Zhang, J. Feng and S. Xiong, *Adv. Energy Mater.*, 2018, **8**, 1703242.
30 S. Wang, J. Teng, Y. Xie, Z.-W. Wei, Y. Fan, J.-J. Jiang, H.-P. Wang, H. Liu, D. Wang and C.-Y. Su, *J. Mater. Chem. A*, 2019, **7**, 4036–4046.
31 K. Wang, H. Chen, Y. Hua, Y. Tong, Y. Wang and S. Song, *Mater. Today Energy*, 2018, **10**, 343–351.
32 Q. Lu, Y. Yu, Q. Ma, B. Chen and H. Zhang, *Adv. Mater.*, 2016, **28**, 1917–1933.
33 W. Sun, Y. Du, G. Wu, G. Gao, H. Zhu, J. Shen, K. Zhang and G. Cao, *J. Mater. Chem. A*, 2019, **7**, 7138–7150.
34 R. Wang, X.-Y. Dong, J. Du, J.-Y. Zhao and S.-Q. Zang, *Adv. Mater.*, 2018, **30**, 1703711.
35 K. Wang, C. Wu, F. Wang and G. Jiang, *ACS Appl. Nano Mater.*, 2018, **1**, 5843–5853.
36 M. Zhai, F. Wang and H. Du, *ACS Appl. Mater. Interfaces*, 2017, **9**, 40171–40179.
37 J.-S. Li, S. Zhang, J.-Q. Sha, H. Wang, M. Z. Liu, L.-X. Kong and G.-D. Liu, *ACS Appl. Mater. Interfaces*, 2018, **10**, 17140–17146.
38 X. Fan, C. Yu, J. Yang, Z. Ling, C. Hu, M. Zhang and J. Qiu, *Adv. Energy Mater.*, 2015, **5**, 1401761.
39 T. He, B. Ni, Y. Ou, H. Lin, S. Zhang, C. Li, J. Zhuang, W. Hu and X. Wang, *Small Methods*, 2018, **2**, 1800068.
40 L. Cao, T. Wang and C. Wang, *Chin. J. Chem.*, 2018, **36**, 754–764.
41 S. Stepanow, N. Lin, D. Payer, U. Schlickum, F. Klappenberger, G. Zoppellaro, M. Ruben, H. Brune, J. V. Barth and K. Kern, *Angew. Chem., Int. Ed.*, 2007, **46**, 710–713.
42 W. Liu, R. Yin, X. Xu, L. Zhang, W. Shi and X. Cao, *Adv. Sci.*, 2019, **6**, 1802373.
43 K. S. Novoselov, A. K. Geim, S. V. Morozov, D. Jiang, Y. Zhang, S. V. Dubonos, I. V. Grigorieva and A. A. Firsov, *Science*, 2004, **306**, 666–669.

44 F. Bonaccorso, L. Colombo, G. Yu, M. Stoller, V. Tozzini, A. C. Ferrari, R. S. Ruoff and V. Pellegrini, *Science*, 2015, **347**, 1246501.
45 A. K. Geim and K. S. Novoselov, *Nat. Mater.*, 2007, **6**, 183–191.
46 J. Hou, K. Jiang, M. Tahir, X. Wu, F. Idrees, M. Shen and C. Cao, *J. Power Sources*, 2017, **371**, 148–155.
47 Z.-X. Li, B.-L. Yang, K.-Y. Zou, L. Kong, M.-L. Yue and H.-H. Duan, *Carbon*, 2019, **144**, 540–548.
48 C. Li, H. Liu and Z. Yu, *Appl. Catal., B*, 2019, **241**, 95–103.
49 F. Tu, Y. Han, Y. Du, X. Ge, W. Weng, X. Zhou and J. Bao, *ACS Appl. Mater. Interfaces*, 2019, **11**, 2112–2119.
50 S. Manzeli, D. Ovchinnikov, D. Pasquier, O. V. Yazyev and A. Kis, *Nat. Rev. Mater.*, 2017, **2**, 17033.
51 L. Li, Y. Yu, G. J. Ye, Q. Ge, X. Ou, H. Wu, D. Feng, X. H. Chen and Y. Zhang, *Nat. Nanotechnol.*, 2014, **9**, 372–377.
52 M. Buscema, D. J. Groenendijk, S. I. Blanter, G. A. Steele, H. S. J. van der Zant and A. Castellanos-Gomez, *Nano Lett.*, 2014, **14**, 3347–3352.
53 Q. Weng, X. Wang, X. Wang, Y. Bando and D. Golberg, *Chem. Soc. Rev.*, 2016, **45**, 3989–4012.
54 Y. Xia, T. S. Mathis, M.-Q. Zhao, B. Anasori, A. Dang, Z. Zhou, H. Cho, Y. Gogotsi and S. Yang, *Nature*, 2018, **557**, 409–412.
55 M. Zhao, Y. Huang, Y. Peng, Z. Huang, Q. Ma and H. Zhang, *Chem. Soc. Rev.*, 2018, **47**, 6267–6295.
56 H. Liu, X. Li, L. Chen, X. Wang, H. Pan, X. Zhang and M. Zhao, *J. Phys. Chem. C*, 2016, **120**, 3846–3852.
57 M. Zhang, G. Feng, Z. Song, Y.-P. Zhou, H.-Y. Chao, D. Yuan, T. T. Y. Tan, Z. Guo, Z. Hu, B. Z. Tang, B. Liu and D. Zhao, *J. Am. Chem. Soc.*, 2014, **136**, 7241–7244.
58 S. Liu, D. Li, G. Zhang, D. Sun, J. Zhou and H. Song, *ACS Appl. Mater. Interfaces*, 2018, **10**, 34193–34201.
59 W. Zhao, J. Peng, W. Wang, S. Liu, Q. Zhao and W. Huang, *Coord. Chem. Rev.*, 2018, **377**, 44–63.
60 L. Huang, X. Zhang, Y. Han, Q. Wang, Y. Fang and S. Dong, *J. Mater. Chem. A*, 2017, **5**, 18610–18617.
61 J. Liu, H. Yu, L. Wang, Z. Deng, K.-u.-R. Naveed, A. Nazir and F. Haq, *Inorg. Chim. Acta*, 2018, **483**, 550–564.
62 M. Zhao, Q. Lu, Q. Ma and H. Zhang, *Small Methods*, 2017, **1**, 1600030.
63 Y.-z. Li, Z.-h. Fu and G. Xu, *Coord. Chem. Rev.*, 2019, **388**, 79–106.
64 J. Wang, S. Li, R. Lin, G. Tu, J. Wang and Z. Li, *Electrochim. Acta*, 2019, **301**, 258–266.
65 Y. Peng, Y. Li, Y. Ban and W. Yang, *Angew. Chem., Int. Ed.*, 2017, **56**, 9757–9761.
66 S. C. Junggeburth, L. Diehl, S. Werner, V. Duppel, W. Sigle and B. V. Lotsch, *J. Am. Chem. Soc.*, 2013, **135**, 6157–6164.
67 X. M. Li, L. Tao, Z. F. Chen, H. Fang, X. S. Li, X. R. Wang, J. B. Xu and H. W. Zhu, *Appl. Phys. Rev.*, 2017, **4**, 021306.
68 Z. Liang, C. Qu, D. Xia, R. Zou and Q. Xu, *Angew. Chem., Int. Ed.*, 2018, **57**, 9604–9633.
69 P.-Z. Li, Y. Maeda and Q. Xu, *Chem. Commun.*, 2011, **47**, 8436–8438.
70 P. Amo-Ochoa, L. Welte, R. Gonzalez-Prieto, P. J. Sanz Miguel, C. J. Gomez-Garcia, E. Mateo-Marti, S. Delgado, J. Gomez-Herrero and F. Zamora, *Chem. Commun.*, 2010, **46**, 3262–3264.
71 H. F. Clausen, R. D. Poulsen, A. D. Bond, M.-A. S. Chevallier and B. B. Iversen, *J. Solid State Chem.*, 2005, **178**, 3342–3351.
72 J. A. Foster, S. Henke, A. Schneemann, R. A. Fischer and A. K. Cheetham, *Chem. Commun.*, 2016, **52**, 10474–10477.
73 C. Hermosa, B. R. Horrocks, J. I. Martínez, F. Liscio, J. Gómez-Herrero and F. Zamora, *Chem. Sci.*, 2015, **6**, 2553–2558.
74 Y. Ding, Y.-P. Chen, X. Zhang, L. Chen, Z. Dong, H.-L. Jiang, H. Xu and H.-C. Zhou, *J. Am. Chem. Soc.*, 2017, **139**, 9136–9139.
75 M. J. Cliffe, E. Castillo-Martinez, Y. Wu, J. Lee, A. C. Forse, F. C. N. Firth, P. Z. Moghadam, D. Fairen-Jimenez, M. W. Gaultois, J. A. Hill, O. V. Magdysyuk, B. Slater, A. L. Goodwin and C. P. Grey, *J. Am. Chem. Soc.*, 2017, **139**, 5397–5404.
76 A. Dmitriev, H. Spillmann, N. Lin, J. V. Barth and K. Kern, *Angew. Chem., Int. Ed.*, 2003, **42**, 2670–2673.
77 J. Huang, Y. Li, R.-K. Huang, C.-T. He, L. Gong, Q. Hu, L. Wang, Y.-T. Xu, X.-Y. Tian, S.-Y. Liu, Z.-M. Ye, F. Wang, D.-D. Zhou, W.-X. Zhang and J.-P. Zhang, *Angew. Chem., Int. Ed.*, 2018, **130**, 4722–4726.
78 L.-J. Han, D. Zheng, S.-G. Chen, H.-G. Zheng and J. Ma, *Small*, 2018, **14**, 1703873.
79 R. A. Vilá, K. Momeni, Q. Wang, B. M. Bersch, N. Lu, M. J. Kim, L. Q. Chen and J. A. Robinson, *2D Mater.*, 2016, **3**, 041003.
80 D. Wei, Y. Liu, H. Zhang, L. Huang, B. Wu, J. Chen and G. Yu, *J. Am. Chem. Soc.*, 2009, **131**, 11147–11154.
81 Z. Fan, Y. Liu, J. Yan, G. Ning, Q. Wang, T. Wei, L. Zhi and F. Wei, *Adv. Energy Mater.*, 2012, **2**, 419–424.
82 L. Wan, W. Sun, J. Shen and X. Li, *Electrochim. Acta*, 2016, **211**, 962–971.
83 K. Zhu, J. Sun, H. Zhang, J. Liu and Y. Wang, *J. Nat. Gas Chem.*, 2012, **21**, 215–232.
84 H. Li, J. Hou, T. D. Bennett, J. Liu and Y. Zhang, *J. Mater. Chem. A*, 2019, **7**, 5811–5818.
85 S. J. Limmer, S. Seraji, Y. Wu, T. P. Chou, C. Nguyen and G. Z. Cao, *Adv. Funct. Mater.*, 2002, **12**, 59–64.
86 M. Zhao, Y. Wang, Q. Ma, Y. Huang, X. Zhang, J. Ping, Z. Zhang, Q. Lu, Y. Yu, H. Xu, Y. Zhao and H. Zhang, *Adv. Mater.*, 2015, **27**, 7372–7378.
87 B. Wang, J. Shang, C. Guo, J. Zhang, F. Zhu, A. Han and J. Liu, *Small*, 2019, **15**, 1804761.
88 X. Bai, J. Liu, Q. Liu, R. Chen, X. Jing, B. Li and J. Wang, *Chem.–Eur. J.*, 2017, **23**, 14839–14847.
89 H. Gu, Z. Yang, J. Gao, C. K. Chang and B. Xu, *J. Am. Chem. Soc.*, 2005, **127**, 34–35.
90 R. Makiura, S. Motoyama, Y. Umemura, H. Yamanaka, O. Sakata and H. Kitagawa, *Nat. Mater.*, 2010, **9**, 565–571.
91 R. Makiura and O. Konovalov, *Sci. Rep.*, 2013, **3**, 2506.
92 G. Xu, T. Yamada, K. Otsubo, S. Sakaida and H. Kitagawa, *J. Am. Chem. Soc.*, 2012, **134**, 16524–16527.

93 S. Motoyama, R. Makiura, O. Sakata and H. Kitagawa, *J. Am. Chem. Soc.*, 2011, **133**, 5640–5643.
94 X. Huang, P. Sheng, Z. Tu, F. Zhang, J. Wang, H. Geng, Y. Zou, C.-a. Di, Y. Yi, Y. Sun, W. Xu and D. Zhu, *Nat. Commun.*, 2015, **6**, 7408.
95 D. J. Ashworth and J. A. Foster, *J. Mater. Chem. A*, 2018, **6**, 16292–16307.
96 R. Sakamoto, K. Hoshiko, Q. Liu, T. Yagi, T. Nagayama, S. Kusaka, M. Tsuchiya, Y. Kitagawa, W.-Y. Wong and H. Nishihara, *Nat. Commun.*, 2015, **6**, 6713.
97 T. Rodenas, I. Luz, G. Prieto, B. Seoane, H. Miro, A. Corma, F. Kapteijn, F. X. Llabrés i Xamena and J. Gascon, *Nat. Mater.*, 2014, **14**, 48–55.
98 L. Sun, C. Wang, X. Wang and L. Wang, *Small*, 2018, **14**, 1800090.
99 X. Zhang, P. Zhang, C. Chen, J. Zhang, G. Yang, L. Zheng, J. Zhang and B. Han, *Green Chem.*, 2019, **21**, 54–58.
100 L. Cao, Z. Lin, F. Peng, W. Wang, R. Huang, C. Wang, J. Yan, J. Liang, Z. Zhang, T. Zhang, L. Long, J. Sun and W. Lin, *Angew. Chem., Int. Ed.*, 2016, **55**, 4962–4966.
101 K. Zhao, S. Liu, G. Ye, Q. Gan, Z. Zhou and Z. He, *J. Mater. Chem. A*, 2018, **6**, 2166–2175.
102 K. Zhao, Z. Xu, Z. He, G. Ye, Q. Gan, Z. Zhou and S. Liu, *J. Mater. Sci.*, 2018, **53**, 13111–13125.
103 K. Zhao, S. Liu, G. Ye, X. Wei, Y. Su, W. Zhu, Z. Zhou and Z. He, *ChemSusChem*, 2020, DOI: 10.1002/cssc.201902776.
104 Y. Wang, L. Li, L. Yan, X. Gu, P. Dai, D. Liu, J. G. Bell, G. Zhao, X. Zhao and K. M. Thomas, *Chem. Mater.*, 2018, **30**, 3048–3059.
105 J. Zha and X. Zhang, *Cryst. Growth Des.*, 2018, **18**, 3209–3214.
106 S. He, Y. Chen, Z. Zhang, B. Ni, W. He and X. Wang, *Chem. Sci.*, 2016, **7**, 7101–7105.
107 M. Ko, L. Mendecki and K. A. Mirica, *Chem. Commun.*, 2018, **54**, 7873–7891.
108 G. Jia, S. Liu, G. Yang, F. Li, K. Wu, Z. He and X. Shangguan, *Ionics*, 2019, **25**, 399–410.
109 Q. Gan, J. Xie, Y. Zhu, F. Zhang, P. Zhang, Z. He and S. Liu, *ACS Appl. Mater. Interfaces*, 2019, **11**, 930–939.
110 Q. Gan, K. Zhao, Z. He, S. Liu and A. Li, *J. Power Sources*, 2018, **384**, 187–195.
111 Q. Gan, H. He, K. Zhao, Z. He, S. Liu and S. Yang, *ACS Appl. Mater. Interfaces*, 2018, **10**, 7031–7042.
112 Q. Liu, L. Yu, Y. Wang, Y. Ji, J. Horvat, M.-L. Cheng, X. Jia and G. Wang, *Inorg. Chem.*, 2013, **52**, 2817–2822.
113 Y. Wang, Q. Qu, G. Liu, V. S. Battaglia and H. Zheng, *Nano Energy*, 2017, **39**, 200–210.
114 G. Ferey, F. Millange, M. Morcrette, C. Serre, M. L. Doublet, J. M. Greneche and J. M. Tarascon, *Angew. Chem., Int. Ed.*, 2007, **46**, 3259–3263.
115 C. Li, X. Hu, W. Tong, W. Yan, X. Lou, M. Shen and B. Hu, *ACS Appl. Mater. Interfaces*, 2017, **9**, 29829–29838.
116 J. Jin, Y. Zheng, S.-z. Huang, P.-p. Sun, N. Srikanth, L. B. Kong, Q. Yan and K. Zhou, *J. Mater. Chem. A*, 2019, **7**, 783–790.
117 K. Zhao, S. Liu, Y. Wu, K. Lv, H. Yuan and Z. He, *Electrochim. Acta*, 2015, **174**, 1234–1243.
118 R. Abazari, S. Sanati, A. Morsali, A. M. Z. Slawin, C. L. Carpenter-Warren, W. Chen and A. Zheng, *J. Mater. Chem. A*, 2019, **7**, 11953–11966.
119 D. Feng, T. Lei, M. R. Lukatskaya, J. Park, Z. Huang, M. Lee, L. Shaw, S. Chen, A. A. Yakovenko, A. Kulkarni, J. Xiao, K. Fredrickson, J. B. Tok, X. Zou, Y. Cui and Z. Bao, *Nat. Energy*, 2018, **3**, 30–36.
120 Y. Zheng, S. Zheng, Y. Xu, H. Xue, C. Liu and H. Pang, *Chem. Eng. J.*, 2019, **373**, 1319–1328.
121 J. Park, A. C. Hinckley, Z. Huang, D. Feng, A. A. Yakovenko, M. Lee, S. Chen, X. Zou and Z. Bao, *J. Am. Chem. Soc.*, 2018, **140**, 14533–14537.
122 J. Park, M. Lee, D. Feng, Z. Huang, A. C. Hinckley, A. Yakovenko, X. Zou, Y. Cui and Z. Bao, *J. Am. Chem. Soc.*, 2018, **140**, 10315–10323.
123 Y. Xu, Z. Lin, X. Zhong, X. Huang, N. O. Weiss, Y. Huang and X. Duan, *Nat. Commun.*, 2014, **5**, 4554.
124 T. Lin, I.-W. Chen, F. Liu, C. Yang, H. Bi, F. Xu and F. Huang, *Science*, 2015, **350**, 1508–1513.
125 D. Sheberla, J. C. Bachman, J. S. Elias, C.-J. Sun, Y. Shao-Horn and M. Dinca, *Nat. Mater.*, 2017, **16**, 220–224.
126 J. A. Koza, Z. He, A. S. Miller and J. A. Switzer, *Chem. Mater.*, 2012, **24**, 3567–3573.
127 S. Han, S. Liu, R. Wang, X. Liu, L. Bai and Z. He, *ACS Appl. Mater. Interfaces*, 2017, **9**, 17186–17194.
128 M. K. Bates, Q. Jia, H. Doan, W. Liang and S. Mukerjee, *ACS Catal.*, 2016, **6**, 155–161.
129 Y. Zhang, H. Zhang, J. Yang, Y. Bai, H. Qiu and Y. Wang, *ACS Appl. Mater. Interfaces*, 2016, **8**, 11396–11402.
130 G. Jia, S. Liu, G. Yang, F. Li, K. Wu, Z. He and X. Shangguan, *Ionics*, 2018, **24**, 3705–3715.
131 Y. Xu, B. Li, S. Zheng, P. Wu, J. Zhan, H. Xue, Q. Xu and H. Pang, *J. Mater. Chem. A*, 2018, **6**, 22070–22076.
132 X. Li, D. D. Ma, C. Cao, R. Zou, Q. Xu, X. T. Wu and Q. L. Zhu, *Small*, 2019, **15**, 1902218.
133 F. Sun, G. Wang, Y. Ding, C. Wang, B. Yuan and Y. Lin, *Adv. Energy Mater.*, 2018, **8**, 1800584.
134 S. Zhao, Y. Wang, J. Dong, C.-T. He, H. Yin, P. An, K. Zhao, X. Zhang, C. Gao, L. Zhang, J. Lv, J. Wang, J. Zhang, A. M. Khattak, N. A. Khan, Z. Wei, J. Zhang, S. Liu, H. Zhao and Z. Tang, *Nat. Energy*, 2016, **1**, 1–10.
135 R. Yang, Y. M. Zhou, Y. Y. Xing, D. Li, D. L. Jiang, M. Chen, W. D. Shi and S. Q. Yuan, *Appl. Catal., B*, 2019, **253**, 131–139.
136 W. Zhou, D. D. Huang, Y. P. Wu, J. Zhao, T. Wu, J. Zhang, D. S. Li, C. H. Sun, P. Y. Feng and X. H. Bu, *Angew. Chem., Int. Ed.*, 2019, **58**, 4227–4231.
137 M. T. Lu, Y. W. Li, P. P. He, J. K. Cong, D. N. Chen, J. W. Wang, Y. H. Wu, H. Xu, J. K. Gao and J. M. Yao, *J. Solid State Chem.*, 2019, **272**, 32–37.
138 K. Rui, G. Zhao, Y. Chen, Y. Lin, Q. Zhou, J. Chen, J. Zhu, W. Sun, W. Huang and S. X. Dou, *Adv. Funct. Mater.*, 2018, **28**, 1801554.
139 G. Hai, X. Jia, K. Zhang, X. Liu, Z. Wu and G. Wang, *Nano Energy*, 2018, **44**, 345–352.
140 K. Jayaramulu, J. Masa, D. M. Morales, O. Tomanec, V. Ranc, M. Petr, P. Wilde, Y.-T. Chen, R. Zboril,

W. Schuhmann and R. A. Fischer, *Adv. Sci.*, 2018, **5**, 1801029.
141 M. Ding, J. Chen, M. Jiang, X. Zhang and G. Wang, *J. Mater. Chem. A*, 2019, **7**, 14163–14168.
142 C. A. Downes, A. J. Clough, K. Chen, J. W. Yoo and S. C. Marinescu, *ACS Appl. Mater. Interfaces*, 2018, **10**, 1719–1727.
143 R. Dong, M. Pfeffermann, H. Liang, Z. Zheng, X. Zhu, J. Zhang and X. Feng, *Angew. Chem., Int. Ed.*, 2015, **54**, 12058–12063.
144 R. Dong, Z. Zheng, D. C. Tranca, J. Zhang, N. Chandrasekhar, S. Liu, X. Zhuang, G. Seifert and X. Feng, *Chem.–Eur. J.*, 2017, **23**, 2255–2260.
145 X. Dai, M. Liu, Z. Li, A. Jin, Y. Ma, X. Huang, H. Sun, H. Wang and X. Zhang, *J. Phys. Chem. C*, 2016, **120**, 12539–12548.
146 J. Duan, S. Chen and C. Zhao, *Nat. Commun.*, 2017, **8**, 15341.
147 X. Wei, N. Li and N. Liu, *Electrochim. Acta*, 2019, **318**, 957–965.
148 C.-W. Tung, Y.-Y. Hsu, Y.-P. Shen, Y. Zheng, T.-S. Chan, H.-S. Sheu, Y.-C. Cheng and H. M. Chen, *Nat. Commun.*, 2015, **6**, 8106.
149 X. L. Xing, R. J. Liu, K. C. Cao, U. Kaiser and C. Streb, *Chem.–Eur. J.*, 2019, **25**, 11098.
150 J. Y. Liu, H. Xu, H. P. Li, Y. H. Song, J. J. Wu, Y. J. Gong, L. Xu, S. Q. Yuan, H. M. Li and P. M. Ajayan, *Appl. Catal., B*, 2019, **243**, 151–160.
151 Y. Li, Z. Qiao, Y. Cao, H. Wang, H. Liang, H. Yu and F. Peng, *ChemSusChem*, 2019, **12**, 1133–1138.
152 R. Z. Gao, Y. H. Yin, F. Q. Niu, A. L. Wang, S. Y. Li, H. Y. Dong and S. T. Yang, *ChemElectroChem*, 2019, **6**, 1824–1830.
153 G. Li, S. Zhao, Y. Zhang and Z. Tang, *Adv. Mater.*, 2018, **30**, 1800702.
154 M. Jahan, Q. Bao and K. P. Loh, *J. Am. Chem. Soc.*, 2012, **134**, 6707–6713.
155 J. Mao, L. Yang, P. Yu, X. Wei and L. Mao, *Electrochem. Commun.*, 2012, **19**, 29–31.
156 K. Cho, S.-H. Han and M. P. Suh, *Angew. Chem., Int. Ed.*, 2016, **55**, 15301–15305.
157 H. Wang, F.-X. Yin, B.-H. Chen, X.-B. He, P.-L. Lv, C.-Y. Ye and D.-J. Liu, *Appl. Catal., B*, 2017, **205**, 55–67.
158 M. Jahan, Z. Liu and K. P. Loh, *Adv. Funct. Mater.*, 2013, **23**, 5363–5372.
159 E. M. Miner, T. Fukushima, D. Sheberla, L. Sun, Y. Surendranath and M. Dincă, *Nat. Commun.*, 2016, **7**, 10942.
160 H. X. Zhong, K. H. Ly, M. C. Wang, Y. Krupskaya, X. C. Han, J. C. Zhang, J. Zhang, V. Kataev, B. Buchner, I. M. Weidinger, S. Kaskel, P. Liu, M. W. Chen, R. H. Dong and X. L. Feng, *Angew. Chem., Int. Ed.*, 2019, **58**, 10677–10682.
161 W. Lu, X. Li, F. Wei, K. Cheng, W. Li, Y. Zhou, W. Zheng, L. Pan and G. Zhang, *ACS Sustainable Chem. Eng.*, 2019, **7**, 12501–12509.
162 A. J. Clough, J. W. Yoo, M. H. Mecklenburg and S. C. Marinescu, *J. Am. Chem. Soc.*, 2015, **137**, 118–121.
163 X. Sun, K.-H. Wu, R. Sakamoto, T. Kusamoto, H. Maeda, X. Ni, W. Jiang, F. Liu, S. Sasaki, H. Masunaga and H. Nishihara, *Chem. Sci.*, 2017, **8**, 8078–8085.
164 B. Qin, Y. Li, H. Wang, G. Yang, Y. Cao, H. Yu, Q. Zhang, H. Liang and F. Peng, *Nano Energy*, 2019, **60**, 43–51.
165 W. Zheng, C.-S. Tsang, L. Y. S. Lee and K.-Y. Wong, *Mater. Today Chem.*, 2019, **12**, 34–60.
166 R. Wang, X. Sun, S. Ould-Chikh, D. Osadchii, F. Bai, F. Kapteijn and J. Gascon, *ACS Appl. Mater. Interfaces*, 2018, **10**, 14751–14758.
167 W. Zhu, K. Zhao, S. Liu, M. Liu, F. Peng, P. An, B. Qin, H. Zhou, H. Li and Z. He, *J. Energy Chem.*, 2019, **37**, 176–182.
168 F. N. Al-Rowaili, A. Jamal, M. S. Ba Shammakh and A. Rana, *ACS Sustainable Chem. Eng.*, 2018, **6**, 15895–15914.
169 N. Kornienko, Y. Zhao, C. S. Kley, C. Zhu, D. Kim, S. Lin, C. J. Chang, O. M. Yaghi and P. Yang, *J. Am. Chem. Soc.*, 2015, **137**, 14129–14135.
170 J. Shen, R. Kortlever, R. Kas, Y. Y. Birdja, O. Diaz-Morales, Y. Kwon, I. Ledezma-Yanez, K. J. P. Schouten, G. Mul and M. T. M. Koper, *Nat. Commun.*, 2015, **6**, 8177.
171 X. Han, L. Sun, F. Wang and D. Sun, *J. Mater. Chem. A*, 2018, **6**, 18891–18897.
172 G. P. Hao, C. Tang, E. Zhang, P. Zhai, J. Yin, W. Zhu, Q. Zhang and S. Kaskel, *Adv. Mater.*, 2017, **29**, 1702829.
173 H. Cao, S. Zhu, C. Yang, R. Bao, L. Tong, L. Hou, X. Zhang and C. Yuan, *Nanotechnology*, 2016, **27**, 465402.
174 G. Fang, J. Zhou, Y. Cai, S. Liu, X. Tan, A. Pan and S. Liang, *J. Mater. Chem. A*, 2017, **5**, 13983–13993.
175 S. Liu, J. Zhou and H. Song, *Adv. Energy Mater.*, 2018, **8**, 1800569.
176 Y. Dong, W. Shi, P. Lu, J. Qin, S. Zheng, B. Zhang, X. Bao and Z.-S. Wu, *J. Mater. Chem. A*, 2018, **6**, 14324–14329.
177 D. Sun, S. Liu, G. Zhang and J. Zhou, *Chem. Eng. J.*, 2019, **359**, 1659–1667.
178 F. Cao, M. Zhao, Y. Yu, B. Chen, Y. Huang, J. Yang, X. Cao, Q. Lu, X. Zhang, Z. Zhang, C. Tan and H. Zhang, *J. Am. Chem. Soc.*, 2016, **138**, 6924–6927.
179 C. Guan, W. Zhao, Y. Hu, Z. Lai, X. Li, S. Sun, H. Zhang, A. K. Cheetham and J. Wang, *Nanoscale Horiz.*, 2017, **2**, 99–105.
180 M. Nagalakshmi and N. Kalaiselvi, *Electrochim. Acta*, 2019, **304**, 175–183.
181 H. Wen, C. Shi, Y. Gao, H. Rong, Y. Sha, H. Liu and Q. Liu, *Nano*, 2019, **13**, 1850139.
182 B.-W. Hu, Y.-J. Zhu, L. Du, T.-S. Mu, W.-Q. Zhu, G.-P. Yin, P. Chen and Q.-W. Li, *Inorg. Chim. Acta*, 2019, **494**, 1–7.
183 T. Wang, Z. Kou, S. Mu, J. Liu, D. He, I. S. Amiinu, W. Meng, K. Zhou, Z. Luo, S. Chaemchuen and F. Verpoort, *Adv. Funct. Mater.*, 2018, **28**, 1705048.
184 S. Liao, Y. Sun, J. Wang, H. Cui and C. Wang, *Electrochim. Acta*, 2016, **211**, 11–17.
185 W. Bao, Z. Zhang, Y. Qu, C. Zhou, X. Wang and J. Li, *J. Alloys Compd.*, 2014, **582**, 334–340.

186 J. Zhao, X. Yang, Y. Yao, Y. Gao, Y. Sui, B. Zou, H. Ehrenberg, G. Chen and F. Du, *Adv. Sci.*, 2018, **5**, 1700768.
187 R. Bi, C. Zeng, H. Huang, X. Wang and L. Zhang, *J. Mater. Chem. A*, 2018, **6**, 14077–14082.
188 Y. Cai, G. Fang, J. Zhou, S. Liu, Z. Luo, A. Pan, G. Cao and S. Liang, *Nano Res.*, 2018, **11**, 449–463.
189 S. Liu, J. Zhou and H. Song, *Chem. Commun.*, 2018, **54**, 9825–9828.
190 M. Huang, K. Mi, J. Zhang, H. Liu, T. Yu, A. Yuan, Q. Kong and S. Xiong, *J. Mater. Chem. A*, 2017, **5**, 266–274.
191 R. Wu, D. P. Wang, V. Kumar, K. Zhou, A. W. K. Law, P. S. Lee, J. Lou and Z. Chen, *Chem. Commun.*, 2015, **51**, 3109–3112.
192 K. Chen, Z. Sun, R. Fang, Y. Shi, H.-M. Cheng and F. Li, *Adv. Funct. Mater.*, 2018, **28**, 1707592.
193 S. Liu, M. Tong, G. Liu, X. Zhang, Z. Wang, G. Wang, W. Cai, H. Zhang and H. Zhao, *Inorg. Chem. Front.*, 2017, **4**, 491–498.
194 H. Han, Z. Bai, X. Wang, S. Chao, J. Liu, Q. Kong, X. Yang and L. Yang, *Catal. Today*, 2018, **318**, 126–131.
195 H. Furukawa, K. E. Cordova, M. O'Keeffe and O. M. Yaghi, *Science*, 2013, **341**, 1230444.
196 H. Zou, B. He, P. Kuang, J. Yu and K. Fan, *ACS Appl. Mater. Interfaces*, 2018, **10**, 22311–22319.
197 M. Jiang, J. Li, X. Cai, Y. Zhao, L. Pan, Q. Cao, D. Wang and Y. Du, *Nanoscale*, 2018, **10**, 19774–19780.
198 Y. Xu, W. Tu, B. Zhang, S. Yin, Y. Huang, M. Kraft and R. Xu, *Adv. Mater.*, 2017, **29**, 1605957.
199 T. Huang, Y. Chen and J.-M. Lee, *ACS Sustainable Chem. Eng.*, 2017, **5**, 5646–5650.
200 F. Yang, Y. Chen, G. Cheng, S. Chen and W. Luo, *ACS Catal.*, 2017, **7**, 3824–3831.
201 J.-S. Li, S.-L. Li, Y.-J. Tang, M. Han, Z.-H. Dai, J.-C. Bao and Y.-Q. Lan, *Chem. Commun.*, 2015, **51**, 2710–2713.
202 W. Xia, J. Li, T. Wang, L. Song, H. Guo, H. Gong, C. Jiang, B. Gao and J. He, *Chem. Commun.*, 2018, **54**, 1623–1626.
203 L. Liu, G. Zeng, J. Chen, L. Bi, L. Dai and Z. Wen, *Nano Energy*, 2018, **49**, 393–402.
204 J. Cao, C. Lei, J. Yang, X. Cheng, Z. Li, B. Yang, X. Zhang, L. Lei, Y. Hou and K. Ostrikov, *J. Mater. Chem. A*, 2018, **6**, 18877–18883.
205 Y. Jiang, H. Liu, X. Tan, L. Guo, J. Zhang, S. Liu, Y. Guo, J. Zhang, H. Wang and W. Chu, *ACS Appl. Mater. Interfaces*, 2017, **9**, 25239–25249.
206 S. Li, C. Cheng, H.-W. Liang, X. Feng and A. Thomas, *Adv. Mater.*, 2017, **29**, 1700707.
207 Z. Li, M. Shao, L. Zhou, R. Zhang, C. Zhang, M. Wei, D. G. Evans and X. Duan, *Adv. Mater.*, 2016, **28**, 2337–2344.
208 Q. Zuo, T. Liu, C. Chen, Y. Ji, X. Gong, Y. Mai and Y. Zhou, *Angew. Chem., Int. Ed.*, 2019, **58**, 10198–10203.
209 X. Wang, P. Li, Z. Li, W. Chen, H. Zhou, Y. Zhao, X. Wang, L. Zheng, J. Dong, Y. Lin, X. Zheng, W. Yan, J. Yang, Z. Yang, Y. Qu, T. Yuan, Y. Wu and Y. Li, *Chem. Commun.*, 2019, **55**, 6563–6566.

